Draft version October 9, 2025
Typeset using LATEX **twocolumn** style in AASTeX631

Recovering 3D Magnetic Turbulence from Single-Frequency Faraday Screens: Numerical Validation and an Observer's Recipe

A. Melnichenka ,[1] A. Lazarian,[2] and D. Pogosyan[3]

[1]*Department of Physics, Berea College, USA*
[2]*Department of Astronomy, University of Wisconsin-Madison, USA*
[3]*Department of Physics, University of Alberta, Canada*

(Received October 9, 2025)

Submitted to ApJ

ABSTRACT

We show that magnetized turbulence can be measured from a single polarization map at one radio frequency. We focus on two practical diagnostics that observers can compute directly from the map: (i) the polarization-angle structure function $D_\varphi(R,\lambda) = \frac{1}{2}[1 - e^{-2\lambda^4 D_\Phi(R)}]$, and (ii) the "directional" correlation $S(R) = \langle\cos[2(\chi(\mathbf{x}) - \chi(\mathbf{x}+\mathbf{R}))]\rangle$ which we refer to as the Polarization Angle Directional Correlation (PADC). Using synthetic Faraday screens and Athena MHD simulations, we demonstrate that both recover the inertial-range statistics of the underlying 3-D magnetic field without RM synthesis or broad spectral coverage. The $S(R)$ route—implemented via Fourier power of $\cos 2\chi$ and $\sin 2\chi$—mimics an interferometric estimator, avoids angle unwrapping and saturation, and remains robust when large spatial scales are filtered by the instrument response.

For observers with limited frequency coverage, we provide a simple, observable criterion based on the rotation dispersion and wavelength that indicates when a single band suffices, when two nearby bands recover the slope in the transitional regime, and when full multi-frequency synthesis is required. We quantify these regimes on controlled two-slope tests and on Athena snapshots spanning sub- and super-Alfvénic conditions, and we verify the expected 2D from 3D slope mapping under projection. So we could compute $D_\varphi(R)$ or $S(R)$ from one map; check the saturation criterion; if needed, add one adjacent band to restore the turbulence slope.

Unified Astronomy Thesaurus concepts: Interstellar magnetic fields (845); Interstellar medium (847); Intracluster media (858); Interstellar dynamics (839); Magnetohydrodynamics (1964); Turbulence (1735); Faraday rotation (529); Polarimetry (1278); Numerical methods (1965).

1. INTRODUCTION

Magnetic turbulence is ubiquitous in astrophysics (Armstrong et al. 1995). Magentic turbulence shapes star formation (Federrath 2016), angular–momentum (Balbus & Hawley 1991) and mediates heat and cosmic–ray propagation (Brandenburg & Lazarian 2013), yet most observational diagnostics are limited to 2D projections along the line of sight (LOS) (Elmegreen & Scalo 2004). Faraday rotation is one of the most widely used probes of these magnetized plasmas: from Galactic RM grids and pulsars to cluster radio halos and FRBs, it reveals the LOS magnetic field weighted by the thermal-electron density, and—through its spatial statistics—encodes the underlying turbulence (e.g., see the review by Akahori et al. 2018).

The development of the RM synthesis technique (Brentjens & de Bruyn 2005; Burn 1966) has greatly increased the amount of information that can be extracted from polarization observations, as it allows polarized emission to be separated by the degree of Faraday rotation it has experienced.

Recent research has been done: Zhang et al. (2023) with new observation-based techniques, provide numerically test the polarization analysis techniques, Zhang et al. (2016) numerically test the polarization analysis techniques, Xiao et al. (2025) includes the analysis with previous research and has analysis of simulations with white-noise; Herron et al. (2016) studied polarization fluctuation statistics to probe ISM turbulence, and found that power spectra of polarized intensity fluctuations follow a power law.

Earlier work used synchrotron intensity and polarized intensity fluctuations to infer the spectrum and anisotropy of magnetic turbulence (e.g., Getmantsev 1959; Lazarian & Shutenkov 1990; Lazaryan & Chibisov 1991; Waelkens et al. 2009; Junklewitz & Enßlin 2011). Experimental observational data were available, but the theoretical understanding of these processes came with Lazarian & Pogosyan (2012, hereafter LP12), who derived synchrotron statistics for an arbitrary electron index and, crucially, adopted a physically motivated model of anisotropic MHD turbulence consistent with Goldreich & Sridhar (1995).

Before GS95, numerical simulations (e.g., Shebalin et al. 1983; Oughton et al. 1994) suggested scale-independent anisotropy, and this was widely believed to be the case. GS95 introduced the idea that anisotropy should in fact be scale-dependent, becoming stronger at smaller scales: if turbulence is thought of as eddies, then the eddies have different perpendicular and parallel scales.

A limitation of GS95 was that for sub-Alfvénic or trans-Alfvénic turbulence, the anisotropy appeared scale-independent, consistent with earlier numerical simulations (Shebalin et al. 1983; Oughton et al. 1994). This issue was resolved by Lazarian & Vishniac (1999), who studied magnetic reconnection and recovered scale-dependent anisotropy by formulating their model in the local reference frame aligned with the surrounding magnetic field. In this frame, eddies do not interact with the global mean field but instead mix local magnetic fields. This mixing is enabled by fast magnetic reconnection: whereas reconnection was previously thought to be slow, Lazarian & Vishniac (1999) showed that it can be fast, allowing efficient field-line mixing. As a result, scale-dependent anisotropy emerges naturally in the new dynamical local frame.

Subsequent work by Cho & Vishniac (2000) confirmed that the GS95 relations hold only in the local reference frame, establishing a new methodology for analyzing turbulence. Further numerical evidence, including for compressible turbulence, was provided by Cho & Lazarian (2003); Kowal & Lazarian (2010).

Building on this, Lazarian & Pogosyan (2016, hereafter LP16) incorporated Faraday rotation and established how synchrotron polarization statistics depend on the underlying magnetic and electron-density fluctuations along the line of sight.

The measures in LP16, the one that were used by theoreticians, as well as new measures such as D_p and D_λ, were introduced. However, these were not sufficiently sensitive to Faraday rotation.

A key practical question for observers is what turbulence information can be recovered when only a single band (or a few nearby bands) is available. Motivated by this, we introduce a new measure,

$$S(R) = \langle \cos 2[\varphi(\mathbf{x}) - \varphi(\mathbf{x}+\mathbf{R})]\rangle, \tag{1}$$

following Lazarian et al. (2022), and investigate whether it can be used effectively and whether it offers advantages.

We show numerically that $S(R)$ recovers the inertial–range properties of the underlying 3D magnetic turbulence even at a single frequency (cf. Lazarian & Pogosyan 2016; Lazarian & Yuen 2018; Lazarian et al. 2022), without requiring a wavelength array or full interferometric coverage.

There are two main observational scenarios to consider: (i) when the same volume both emits synchrotron radiation and experiences Faraday rotation—i.e., a mixed emitting and rotating medium where classical internal depolarization effects apply (Burn 1966; Sokoloff et al. 1999), (ii) when the synchrotron emission region and the Faraday-rotating medium are spatially separated, as for extragalactic background sources seen through the Milky Way (Brentjens & de Bruyn 2005; Taylor et al. 2009; Oppermann et al. 2012), where synchrotron emission may originate in the galaxy halo (Beck 2015; Haverkorn 2015)—dominated by relativistic electrons but with low thermal electron density—while most Faraday rotation occurs in the denser thermal plasma of the disk (Jansson & Farrar 2012; **?**).

A central question is how Faraday rotation behaves under these conditions when analyzed with the $S(R)$ measure, and whether this statistic can be reliably used. We validate our approach using both synthetic Faraday screens and ATHENA MHD simulations spanning sub- and super-Alfvénic regimes (e.g., Stone et al. 2008, 2020). In the weak-rotation limit we recover the predicted mapping between 3D and plane-of-sky spectra (Lazarian & Pogosyan 2016; Xu & Zhang 2016), while in the transitional regime our single- or two-frequency criteria indicate when reliable recovery is still possible (Lazarian & Yuen 2018; Li et al. 2025). The result is a practical pathway to extract turbulence statistics from single-frequency radio polarimetry and from data sets with incomplete instrumental coverage (Brentjens & de Bruyn 2005; Lazarian & Pogosyan 2016).

We structure the paper as following: Sect. 2 summarizes the obtaining of structure function, Sect. 3 describes obtaining of the directional spectrum, Sect. 6 discusses the results and Sect. 8 gives a conclusive summary.

2. STRUCTURE FUNCTION

A uniform background source emits a complex linear polarization:

$$P_{\rm i} = Q_{\rm i} + iU_{\rm i}, \qquad |P_{\rm i}| = \text{const.} \tag{2}$$

After propagation through a magnetised slab of thickness L the signal is Faraday–rotated by an angle $\lambda^2\Phi(\mathbf{X})$ (classical λ^2 law; Burn 1966; Gardner & Whiteoak 1966), where the Faraday depth (rotation measure) is

$$\Phi(\mathbf{X}) = \int_0^L n_e(\mathbf{X},z) B_z(\mathbf{X},z) dz. \tag{3}$$

The observed complex polarization at sky position $\mathbf{X}$ and wavelength λ is therefore Burn 1966:

$$P(\mathbf{X},\lambda) = P_i e^{2i\lambda^2\Phi(\mathbf{X})}, \tag{4}$$

For two sight lines $\mathbf{X}_1, \mathbf{X}_2$ we define the directional correlation (used in polarization spatial analysis; Lazarian et al. 2022)

$$\begin{aligned} S(R,\lambda) &= \Big\langle \cos\big[\varphi(\mathbf{X}_1) - \varphi(\mathbf{X}_2)\big] \Big\rangle \\ &= \Big\langle \cos\big[2\lambda^2 \Delta\Phi\big] \Big\rangle. \end{aligned} \tag{5}$$

with $\Delta\Phi \equiv \Phi(\mathbf{X}_1) - \Phi(\mathbf{X}_2)$.

2.1. *Angle structure function*

Assume $\Delta\Phi$ is Gaussian, $\langle\Delta\Phi\rangle = 0$, $\langle(\Delta\Phi)^2\rangle = D_\Phi(R)$.

Using the characteristic function of a Gaussian variable (Goodman 1963, Sec. 5.7),

$$\left\langle e^{i2\lambda^2\Delta\Phi}\right\rangle = \exp\left[-2\lambda^4 D_\Phi(R)\right], \tag{6}$$

and therefore

$$S(R,\lambda) = \exp\left[-2\lambda^4 D_\Phi(R)\right]. \tag{7}$$

By definition

$$D_\varphi(R,\lambda) = \frac{1}{2}\Big[1 - S(R,\lambda)\Big] = \frac{1}{2}\Big[1 - e^{-2\lambda^4 D_\Phi(R)}\Big]. \tag{7}$$

For $2\lambda^4 D_\Phi \ll 1$ (weak rotation)

$$D_\varphi(R,\lambda) \simeq \lambda^4 D_\Phi(R). \tag{8}$$

2.2. *Rotation Measure structure function*

Inside the slab the Rotation Measure density has correlation $\langle f(\mathbf{r}) f(\mathbf{0})\rangle \propto r^{-11/3}$ (e.g., Armstrong et al. 1995; Chepurnov & Lazarian 2010; for RM structure functions see Simonetti et al. 1984; Minter & Spangler 1996; Haverkorn 2015). Its two–point integral along z then gives, for $R \ll L$,

$$D_\Phi(R) = 2\sigma_\Phi^2 \kappa \left(\frac{R}{L}\right)^{5/3}, \qquad \kappa = \frac{\sqrt{\pi}\,\Gamma(-5/6)}{2\Gamma(-1/3)}, \tag{9}$$

in agreement with the projected–correlation result $\rho_\perp(R) \approx 1 - \kappa C_2 (R/L)^{5/3}$ from standard projection integrals (Monin & Yaglom 1975, Vol. 2).

Inserting the Kolmogorov D_Φ into (7) (small $R \ll L$) yields

$$D_\varphi(R,\lambda) \approx 2\kappa\sigma_\Phi^2 \lambda^4 \left(\frac{R}{L}\right)^{5/3}. \tag{10}$$

Thus $D_\varphi \propto R^{5/3}$, the same inertial-range slope found for Stokes-azimuth statistics in Eq. (5.26) of the previous work.

For $R \gg L$ the Rotation Measure difference reaches its variance: $D_\Phi \to 2\sigma_\Phi^2$, hence

$$D_\varphi(R,\lambda) \longrightarrow \tfrac{1}{2}\left[1 - e^{-4\lambda^4\sigma_\Phi^2}\right]. \tag{11}$$

$$S(R,\lambda) = e^{-2\lambda^4 D_\Phi(R)}, \tag{12}$$

$$D_\varphi(R,\lambda) = \tfrac{1}{2}\left[1 - e^{-2\lambda^4 D_\Phi(R)}\right]. \tag{13}$$

For a Kolmogorov Rotation Measure screen, $D_\Phi \propto R^{5/3}$ at $R \ll L$. And the angle structure function inherits the same $5/3$ slope (10); at $R \gg L$ it saturates to a constant fixed by the Rotation Measure variance $\sigma_\Phi^2 = \langle \Phi^2\rangle - \langle\Phi\rangle^2$.

3. DIRECTIONAL SPECTRUM

Expresing $\cos 2\phi$, $\sin 2\phi$ in terms of Stokes parameters:

The angle-difference correlation used in your Figure 16 is

$$\begin{aligned} S(R) &= \Big\langle \cos\big(2[\phi(x) - \phi(x+R)]\big)\Big\rangle \\ &= \langle A(x)A(x+R)\rangle + \langle B(x)B(x+R)\rangle. \end{aligned} \tag{14}$$

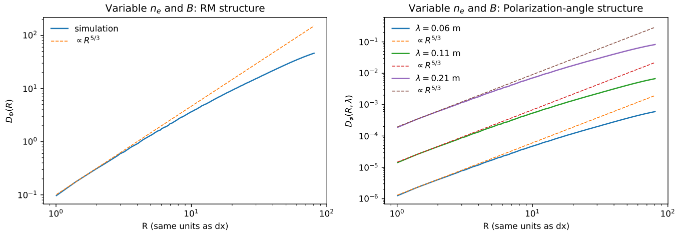

Figure 1. Structure function of the rotation measure calculated by (9) (left) and the polarization angle expressed by (13) (right) for synthetic cube, following Kolmogorov 5/3 scaling. It's clearly visible that the corellation with the analytically predicted $\propto R^{5/3}$ is not well seen for larger R, motivating the need for a more accurate statistical measure.

By Wiener–Khinchin, each scalar correlation is the inverse FFT of its power spectrum:

$$C_A(R) = \langle A(x)A(x+R)\rangle = \mathrm{IFFT}\left[\frac{|\widehat{A}(k)|^2}{N}\right](R). \tag{15}$$

$$C_B(R) = \langle B(x)B(x+R)\rangle = \mathrm{IFFT}\left[\frac{|\widehat{B}(k)|^2}{N}\right](R). \tag{16}$$

$$S(R) = C_A(R) + C_B(R) = \tfrac{1}{N}\,\mathrm{IFFT}\big[|\widehat{A}|^2 + |\widehat{B}|^2\big]. \tag{17}$$

Thus the directional spectrum equation is:

$$P_{\mathrm{dir}}(k) = |\widehat{A}|^2 + |\widehat{B}|^2 = \Big|\mathrm{FFT}\big[(Q+iU)/(pI)\big]\Big|^2. \tag{18}$$

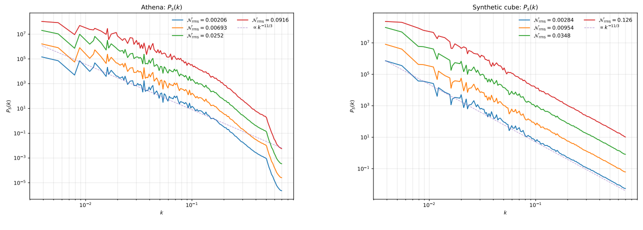

Figure 2. Fourier power spectra of the suggested measure, $P_s(k)$ of $\langle \cos 2f_1 \cos 2f_2 + \sin 2f_1 \sin 2f_2\rangle$. Left: spectrum from the Athena sub-Alfvénic simulation ($M_a = 0.8$) spectrum, Right: spectrum from the synthetically generated cube. At high k, the Athena spectrum shows small drops and partial decorrelation, while the synthetic cube matches the expected scaling exactly.

3.1. *Interferometric high–pass (missing short spacings)*

Interferometers sample the sky in the uv (Fourier) plane, missing short baselines act as a high–pass filter that suppresses large–scale modes. For analytic work we approximate the azimuthally averaged transfer by a smooth radial high–pass, and use a Gaussian proxy that mimics a soft inner uv cutoff:

$$H_{\mathrm{hp}}(k) = 1 - \exp\left(-\frac{k^2}{2k_c^2}\right) \tag{19}$$

The filtered spectrum is

$$\begin{aligned} P_S^{\rm hp}(k) &= |H_{\rm hp}(k)|^2\, P_S(k) \\ &= \big(1 - 2e^{-k^2/2k_c^2} + e^{-k^2/k_c^2}\big) P_S(k). \end{aligned} \tag{20}$$

From the Forier equations standart equation, the inverse transforms of the Gaussians are Gaussians (let $\sigma = k^{-1}$)

$$\begin{cases} F(k) = \int_{\mathbb{R}^2} d^2R\, f(R)\, e^{-ik\cdot R}, \\ f(R) = \dfrac{1}{(2\pi)^2} \int_{\mathbb{R}^2} d^2k\, F(k)\, e^{ik\cdot R} \end{cases} \tag{21}$$

$$\Longrightarrow \begin{cases} \mathcal{F}^{-1}\Big[e^{-k^2/2k_c^2}\Big] = \dfrac{1}{2\pi\sigma^2} e^{-R^2/2\sigma^2}, \\ \mathcal{F}^{-1}\Big[e^{-k^2/k_c^2}\Big] = \dfrac{1}{4\pi\sigma^2} e^{-R^2/4\sigma^2}. \end{cases} \tag{22}$$

Therefore the real-space kernel corresponding to $|H_{\rm hp}|^2$ is

$$h_{\rm hp}(R) = \delta^{(2)}(\mathbf{R}) - \frac{1}{\pi\sigma^2} e^{-R^2/2\sigma^2} + \frac{1}{4\pi\sigma^2} e^{-R^2/4\sigma^2}, \tag{23}$$

thus filtered correlation is the convolution

$$S^{\rm hp}(R) = S(R) - \frac{e^{-R^2/2\sigma^2}}{2\pi\sigma^2}\, S(R) + \frac{e^{-R^2/4\sigma^2}}{4\pi\sigma^2}\, S(R). \tag{24}$$

3.2. *Analytics of the broken power law*

For an isotropic 3D field with spectral density $P_3(k)$, the 1D shell spectrum is

$$E_{\rm 1D}^{(3D)}(k) = 4\pi k^2 P_3(k) \tag{25}$$

Thus if $P_3(k) \propto k^\gamma$, then $E_{\rm 1D}^{(3D)}(k) \propto k^{\gamma+2}$.

We prescribe shell slopes $\alpha_{\rm low} = +3/2$ ($k \ll k_b$) and $\alpha_{\rm high} = -5/3$ ($k \gg k_b$)

$$P_3^{\rm tar}(k) \propto (k/k_b)^{\alpha(k)-2} \tag{26}$$

$$\begin{aligned} \alpha(k) &= \alpha_{\rm low}\, t(k) + \alpha_{\rm high}[1 - t(k)], \\ t(k) &= \frac{1}{1 + (k/k_b)^s}. \end{aligned} \tag{27}$$

so that $E_{\rm 1D}^{(3D)}(k)$ exhibits the desired broken power law. We used $s = 8$ for numerical simulations.

For the plane-of-sky map $g(x, y) = \sum_z f(x, y, z)$, the projection–slice theorem gives $\widehat{g}(k_x, k_y) = \widehat{f}(k_x, k_y, k_z{=}0)$, hence

$$\begin{aligned} P_{\rm 2,proj}(k) &\propto P_3(k) \propto k^\gamma, \\ E_{\rm 1D}^{(2D)}(k) &= 2\pi k\, P_{\rm 2,proj}(k) \propto k^{\gamma+1}. \end{aligned} \tag{28}$$

Combining (25)–(28): if the 3D shell slope is $\alpha^{(3D)}(k) = \gamma + 2$, then the observed 2D slope is

$$\alpha^{(2D)}(k) = \alpha^{(3D)}(k) - 1$$

4. STRUCTURE FUNCTION FOR THE ISOTROPIC MAGNETIC FIELD

By setting $\gamma_{\rm low} = \alpha_{\rm low} - 2 = -\frac{1}{2}$, $\gamma_{\rm high} = \alpha_{\rm high} - 2 = -\frac{11}{3}$ we will get:

$$P_3(k) = C_3 \begin{cases} (k/k_b)^{-1/2}, & k < k_b, \\ (k/k_b)^{-11/3}, & k \ge k_b. \end{cases} \tag{29}$$

2D RM correlation and structure function

$$C_\Phi(R) = 2\pi \int_0^\infty k dk P_\Phi^{(2D)}(k) J_0(kR)$$

$$D_\Phi(R) = 2\left[C_\Phi(0) - C_\Phi(R)\right]$$

Splitting at k_b and defining $x = k_b R$

$$D_\Phi(R) = 4\pi C\left[\frac{\mathcal{I}_{\rm low}(x)}{k_b^{\gamma_{\rm low}} R^{\gamma_{\rm low}+2}} + \frac{\mathcal{I}_{\rm high}(x)}{k_b^{\gamma_{\rm high}} R^{\gamma_{\rm high}+2}}\right]. \tag{30}$$

where $\mathcal{I}_{\rm low}(x) = \int_0^x q^{\gamma_{\rm low}+1}\big(1 - J_0 q\big) dq$ and $\mathcal{I}_{\rm high}(x) = \int_x^\infty q^{\gamma_{\rm high}+1}\big(1 - J_0 q\big) dq$

$$\mathcal{I}_{\rm low}(x) = \frac{x^{\gamma_{\rm low}+2}}{\gamma_{\rm low} + 2}\left[1 - {}_1F_2\Big(\tfrac{\gamma_{\rm low}+2}{2}; 1, \tfrac{\gamma_{\rm low}+4}{2}; -\tfrac{x^2}{4}\Big)\right]. \tag{31}$$

$$\mathcal{I}_{\rm high}(x) = C_{\rm high} - \tfrac{x^{\gamma_{\rm high}+2}}{\gamma_{\rm high}+2}\Big(1 - {}_1F_2(\tfrac{\gamma_{\rm high}+2}{2}; 1, \tfrac{\gamma_{\rm high}+4}{2}; -\tfrac{x^2}{4})\Big). \tag{32}$$

where ${}_1F_2\,(a; b_1, b_2; z) = \sum_{n=0}^\infty \frac{(a)_n}{(b_1)_n (b_2)_n} \frac{z^n}{n!}$ generalized hypergeometric function

$$\begin{aligned} C_{\rm high} &= \int_0^\infty q^{\gamma_{\rm high}+1}\,(1 - J_0 q)\, dq \\ &= \int_0^\infty \frac{1 - J_0 q}{q^{\,1+m}}\, dq = 2^{-m}\, \frac{\Gamma(-\frac{m}{2})}{\Gamma(1 + \frac{m}{2})}. \end{aligned} \tag{33}$$

$m = 5/3$ By normalization

$$\sigma_\Phi^2 = 2\pi C\left[\frac{k_b^{\gamma_{\rm low}+2}}{\gamma_{\rm low} + 2} + \frac{k_b^{\gamma_{\rm high}+2}}{-(\gamma_{\rm high} + 2)}\right]$$

$$C = \frac{\sigma_\Phi^2}{2\pi}\left[\frac{k_b^{\gamma_{\rm low}+2}}{\gamma_{\rm low} + 2} + \frac{k_b^{\gamma_{\rm high}+2}}{-(\gamma_{\rm high} + 2)}\right]^{-1}$$

Remembering $D_\varphi(R, \lambda) = \frac{1}{2}\left[1 - \exp\big(-2\lambda^4 D_\Phi(R)\big)\right]$, the assymptotics:

$$R \ll R_b: \quad D_\Phi(R) \simeq 4\pi C k_b^{-\gamma_{\rm high}} \mathcal{C}_{\rm high} R^{-(\gamma_{\rm high}+2)} \propto R^{5/3}$$

$$R_b \ll R: \quad D_\Phi(R) = 2\sigma_\Phi^2 - A_{\rm low} R^{-(\gamma_{\rm low}+2)} = 2\sigma_\Phi^2 - A_{\rm low} R^{-3/2}$$

5. WHICH SCREEN DOES A GIVEN MEASURE PROBE?

The observed complex polarization at wavelength λ can be written as

$$P(\mathbf{x},\lambda) \;=\; P_0\, e^{2i\,\phi_{\rm em}(\mathbf{x})}\, e^{2i\,\lambda^2\Phi(\mathbf{x})} \tag{34}$$

$$\chi(\mathbf{x},\lambda) \;=\; \phi_{\rm em}(\mathbf{x}) + \lambda^2\Phi(\mathbf{x}) \pmod{\pi} \tag{35}$$

with intrinsic polarization angle $\phi_{\rm em}(\mathbf{x})$. Define the angle correlation

$$S(R,\lambda) \;=\; \big\langle \cos\!\big(2[\chi(\mathbf{x}+\mathbf{R},\lambda)-\chi(\mathbf{x},\lambda)]\big)\big\rangle, \tag{36}$$

and the corresponding angle structure function $D_\chi(R,\lambda) = \frac{1}{2}[1-S(R,\lambda)]$. As was previously shown, the small–increment limit

$$D_\chi(R,\lambda) = D_{\rm em}(R) \;+\; \lambda^4\, D_\Phi(R), \tag{37}$$

including both the emission contribution $D_{\rm em}$ and the Faraday contribution $\lambda^4 D_\Phi$. Thus, for

If we define rotation-dispersion number as $N_{\rm rms} \equiv \frac{\lambda^2\sigma_\Phi}{2\pi}$, the emission–dominated will be with

$$D_{\rm em}(R) \;\gg\; \lambda^4 D_\Phi(R) \quad (\sigma_{\chi,\rm em} \;\gg\; \lambda^2\sigma_\Phi) \tag{38}$$

which usually equalivalent for $N_{\rm RMS} < 0.3$.

Alternatively, Faraday–dominated regime accurs for $D_{\rm em}(R) \;\ll\; \lambda^4 D_\Phi(R)$, with $N_{\rm RMS} \in (0.5, 2.0)$.

6. RESULTS DISCUSSION

Our results demonstrate that turbulence statistics of magnetized plasmas can be recovered robustly from single-frequency polarization data. In particular, we validated two complementary diagnostics: the polarization-angle structure function $D_\varphi(R,\lambda)$ and the directional correlation $S(R)$, both following predicted inertial–range slope.

A key advance is that $S(R)$ avoids angle unwrapping, saturations, and instrumental filtering biases by operating directly on $\cos 2\xi$ and $\sin 2\xi$. This makes it naturally suited to interferometric data sets with incomplete short-spacing coverage, where traditional RM-based approaches can struggle. Our tests on synthetic Kolmogorov screens and Athena simulations spanning sub- and super-Alfvénic regimes confirm that $S(R)$ retains validity to the theoretical $\propto R^{5/3}$ scaling over a wide dynamic range.

7. TRANSITION BETWEEN FARADAY- AND SYNCHROTRON EMITING SCREEN DOMINATED REGIMES

We will examine two regimes: an emission-dominated regime (short λ), where $P_{\rm dir}$ is determined by the synchrotron emissivity structure, and a screen-dominated regime (long λ), where $P_{\rm dir}$ is set by the RM of the Faraday screen. With the transition, happening at $\lambda^2\sigma_{\rm RM}(k) = 1$.

(i) For the external Faraday screen case only, at each λ, the directional spectrum $P_{\rm dir}$ is computed from the complex linear polarization given by $P = e^{2i\lambda^2{\rm RM}}$.

(ii) For both emitting and emission and external screen, a background synchrotron angle field $\psi_{\rm emit}$ independent of λ, and is rotated by the foreground screen,

$$P(x,y;\lambda) = \exp\big(2i[\psi_{\rm emit}(x,y) + \lambda^2{\rm RM}(x,y)]\big).$$

For $\lambda^2\sigma_{\rm RM}(k) \ll 1$, directional spectrum $P_{\rm dir}(k)$ reflects the synchrotron structure; for $\lambda^2\sigma_{\rm RM}(k) > 1$, it reflects the screen statistics.

Let

$$\phi(x;\lambda) = \lambda^2\Phi(x) + \chi(x), \tag{39}$$

$$P(x;\lambda) = Q + iU = \exp\!\big[2i\,\phi(x;\lambda)\big]. \tag{40}$$

Define the directional correlation (the kernel whose 2-D FT gives $P_{\rm dir}$):

$$\mathcal{C}_{\rm dir}(r;\lambda) = \big\langle \cos 2\phi_1\, \cos 2\phi_2 \big\rangle + \big\langle \sin 2\phi_1\, \sin 2\phi_2 \big\rangle, \tag{41}$$

$$r = |x_2 - x_1|. \tag{42}$$

Assume (Φ,χ) are zero-mean, stationary, jointly Gaussian with no cross-correlation:

$$\langle \Phi_i \chi_j \rangle = 0 \quad \forall i,j, \tag{43}$$

$$C = \begin{pmatrix} C_\Phi & 0 \\ 0 & C_\chi \end{pmatrix}, \tag{44}$$

$$C_\Phi = \begin{pmatrix} \langle \Phi_1^2 \rangle & \langle \Phi_1\Phi_2 \rangle \\ \langle \Phi_2\Phi_1 \rangle & \langle \Phi_2^2 \rangle \end{pmatrix}, \tag{45}$$

$$C_\chi = \begin{pmatrix} \langle \chi_1^2 \rangle & \langle \chi_1\chi_2 \rangle \\ \langle \chi_2\chi_1 \rangle & \langle \chi_2^2 \rangle \end{pmatrix}. \tag{46}$$

Using $\cos A\cos B + \sin A \sin B = \cos(A-B)$ and the Gaussian identity $\langle e^{iZ}\rangle = e^{-\frac{1}{2}\,{\rm Var}(Z)}$, with $A = 2(\lambda^2\Phi_1 + \chi_1)$ and $B = 2(\lambda^2\Phi_2 + \chi_2)$,

$$\begin{aligned} \mathcal{C}_{\rm dir}(r;\lambda) &= \exp\Big\{ -4\big[\lambda^4(\sigma_\Phi^2 - \xi_\Phi(r)) + (\sigma_\chi^2 - \xi_\chi(r))\big]\Big\} \\ &= e^{-4(\lambda^4\sigma_\Phi^2 + \sigma_\chi^2)}\, e^{4(\lambda^4\xi_\Phi(r) + \xi_\chi(r))}. \end{aligned} \tag{47}$$

For isotropic fields, the directional spectrum is the Hankel transform

$$P_{\rm dir}(k;\lambda) = 2\pi \int_0^\infty r\, dr\, \mathcal{C}_{\rm dir}(r;\lambda)\, J_0(kr). \tag{48}$$

8. SUMMARY

Practically, $S(R)$ is robust to incomplete frequency sampling and does not require angle unwrapping; D_φ provides a complementary view tied to the familiar RM statistics. Together they give observers a minimal, portable toolkit: with one frequency you can measure turbulence slopes; with sparse coverage you can still form $S(R)$ and compare to inertial–range expectations. We also quantify the limitation from strong Faraday rotation: when typical angle differences exceed 90°, D_φ saturates. We provide a simple, observer–usable criterion—via the dimensionless rotation $\mathcal{N}_{\rm rms} = \lambda^2\sigma_\Phi/(2\pi)$, and we show that adding just one nearby frequency restores the scaling when saturation looms.

REFERENCES

Akahori, T., Nakanishi, H., Sofue, Y., et al. 2018, PASJ, 70, R2, doi: 10.1093/pasj/psx123

Armstrong, J. W., Rickett, B. J., & Spangler, S. R. 1995, ApJ, 443, 209, doi: 10.1086/175515

Balbus, S., & Hawley, J. 1991, The Astrophysical Journal, 376, 214–222

Beck, R. 2015, A&A Rv, 24, 4, doi: 10.1007/s00159-015-0084-4

Brandenburg, A., & Lazarian, A. 2013, Space Science Reviews, 178, 163–200

Brentjens, M. A., & de Bruyn, A. G. 2005, Astronomy & Astrophysics, 441, 1217, doi: 10.1051/0004-6361:20052990

Brentjens, M. A., & de Bruyn, A. G. 2005, A&A, 441, 1217, doi: 10.1051/0004-6361:20052990

Burn, B. J. 1966, Monthly Notices of the Royal Astronomical Society, 133, 67, doi: 10.1093/mnras/133.1.67

Chepurnov, A., & Lazarian, A. 2010, The Astrophysical Journal, 710, 853, doi: 10.1088/0004-637X/710/1/853

Cho, J., & Lazarian, A. 2003, MNRAS, 345, 325, doi: 10.1046/j.1365-8711.2003.06941.x

Cho, J., & Vishniac, E. T. 2000, ApJ, 539, 273, doi: 10.1086/309213

Elmegreen, B. G., & Scalo, J. 2004, ARA&A, 42, 211, doi: 10.1146/annurev.astro.41.011802.094859

Federrath, C. 2016, Journal of Plasma Physics, 82

Gardner, F. F., & Whiteoak, J. B. 1966, ARA&A, 4, 245, doi: 10.1146/annurev.aa.04.090166.001333

Getmantsev, G. G. 1959, Soviet Ast., 3, 415

Goldreich, P., & Sridhar, S. 1995, ApJ, 438, 763, doi: 10.1086/175121

Goodman, N. R. 1963, The Annals of Mathematical Statistics, 34, 152 , doi: 10.1214/aoms/1177704250

Haverkorn, M. 2015, Space Science Reviews, 181, 1, doi: 10.1007/978-3-662-44625-6_17

Herron, C. A., Burkhart, B., Lazarian, A., Gaensler, B. M., & McClure-Griffiths, N. M. 2016, ApJ, 822, 13, doi: 10.3847/0004-637X/822/1/13

Jansson, R., & Farrar, G. R. 2012, ApJ, 757, 14, doi: 10.1088/0004-637X/757/1/14

Junklewitz, H., & Enßlin, T. A. 2011, A&A, 530, A88, doi: 10.1051/0004-6361/201015544

Kowal, G., & Lazarian, A. 2010, ApJ, 720, 742, doi: 10.1088/0004-637X/720/1/742

Lazarian, A., & Pogosyan, D. 2012, ApJ, 747, 5, doi: 10.1088/0004-637X/747/1/5

Lazarian, A., & Pogosyan, D. 2016, Astrophysical Journal, 818, 178, doi: 10.3847/0004-637X/818/2/178

Lazarian, A., & Vishniac, E. T. 1999, ApJ, 517, 700, doi: 10.1086/307233

Lazarian, A., & Yuen, K. 2018, The Astrophysical Journal, 865

Lazarian, A., Yuen, K. H., & Pogosyan, D. 2022, ApJ, 935, 77, doi: 10.3847/1538-4357/ac6877

Lazarian, A. L., & Shutenkov, V. R. 1990, Pisma v Astronomicheskii Zhurnal, 16, 690

Lazaryan, A. L., & Chibisov, G. V. 1991, Soviet Astronomy Letters, 17, 208

Li, R.-N., Zhao, Z.-Y., Wu, Q., Yi, S.-X., & Wang, F.-Y. 2025, The Astrophysical Journal Letters, 979, L41, doi: 10.3847/2041-8213/adabc2

Minter, A. H., & Spangler, S. R. 1996, ApJ, 458, 194, doi: 10.1086/176803

Monin, A. S., & Yaglom, A. M. 1975, Statistical Fluid Mechanics, Vol. 2 (MIT Press)

Oppermann, N., Junklewitz, H., Robbers, G., et al. 2012, A&A, 542, A93, doi: 10.1051/0004-6361/201118526

Oughton, S., Priest, E. R., & Matthaeus, W. H. 1994, Journal of Fluid Mechanics, 280, 95, doi: 10.1017/S0022112094002867

Shebalin, J. V., Matthaeus, W. H., & Montgomery, D. 1983, Journal of Plasma Physics, 29, 525, doi: 10.1017/S0022377800000933

Simonetti, J. H., Cordes, J. M., & Spangler, S. R. 1984, ApJ, 284, 126, doi: 10.1086/162391

Sokoloff, D. D., Bykov, A. A., Shukurov, A., et al. 1999, MNRAS, 303, 207, doi: 10.1046/j.1365-8711.1999.02161.x

Stone, J. M., Gardiner, T. A., Teuben, P., Hawley, J. F., & Simon, J. B. 2008, ApJS, 178, 137, doi: 10.1086/588755

Stone, J. M., Tomida, K., White, C. J., & Felker, K. G. 2020, ApJS, 249, 4, doi: 10.3847/1538-4365/ab929b

Taylor, A. R., Stil, J. M., & Sunstrum, C. 2009, ApJ, 702, 1230, doi: 10.1088/0004-637X/702/2/1230

Waelkens, A. H., Schekochihin, A. A., & Enßlin, T. A. 2009, MNRAS, 398, 1970, doi: 10.1111/j.1365-2966.2009.15231.x

Xiao, Y., Zhang, J., Lazarian, A., & Pogosyan, D. 2025, Influence of Density Distribution on Synchrotron Polarization Dispersion in Magnetized Interstellar Medium. https://arxiv.org/abs/2508.02938

Xu, S., & Zhang, B. 2016, Astrophysical Journal, 824, 113, doi: 10.3847/0004-637X/824/2/113

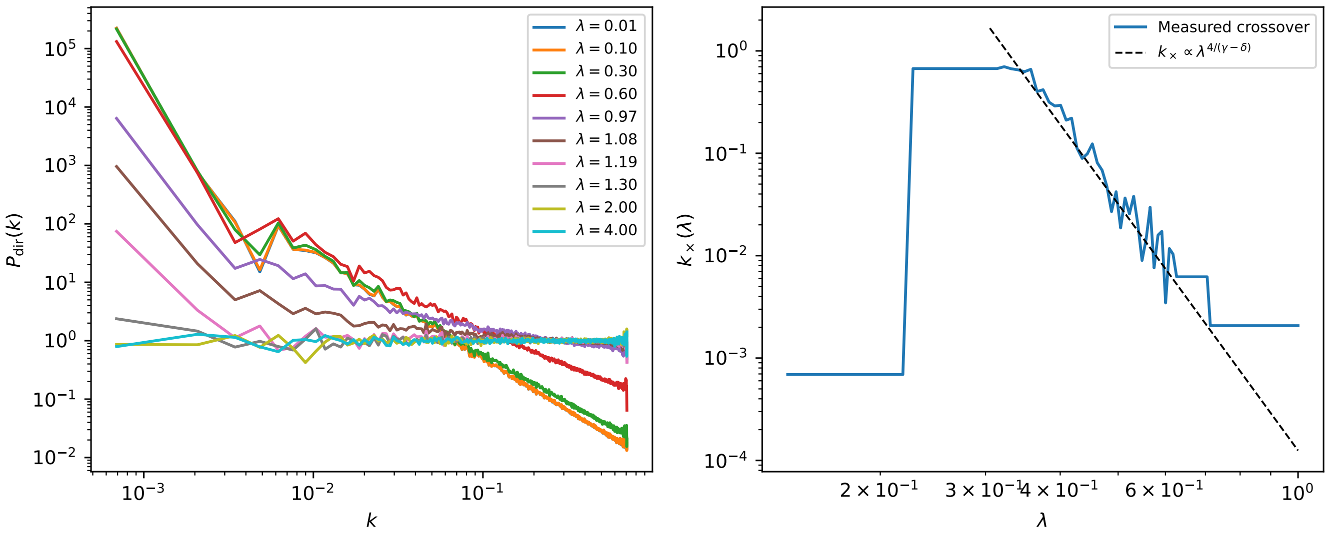

Figure 3. Transition between emission– and Faraday–screen–dominated polarization structure. (a) Directional polarization spectra $P_{\rm dir}(k)$ for ten wavelengths λ. At short λ the spectra follow the synchrotron emission angle field, while at long λ they follow the RM fluctuations of the screen. (b) Crossover wavenumber $k_\times(\lambda)$, defined as the scale where the angle–field powers of $\psi_{\rm emit}$ and $\lambda^2{\rm RM}$ are equal. The dashed line shows the prediction $k_\times \propto \lambda^{4/(\gamma-\delta)}$ based on the measured PSD slopes $P_{\rm RM} \propto k^{-\gamma}$ and $P_\psi \propto k^{-\delta}$ (here $\gamma = 1.3$, $\delta = 1.8$), illustrating the criterion $\lambda^2\sigma_{\rm RM}(k_\times) = 1$.

Zhang, J.-F., Lazarian, A., Lee, H., & Cho, J. 2016, The Astrophysical Journal, 825, 154, doi: 10.3847/0004-637X/825/2/154

Zhang, X.-W., Zhang, J.-F., Wang, R.-Y., & Xiang, F.-Y. 2023, MNRAS, 523, 5748, doi: 10.1093/mnras/stad1785

9. NUMERICAL VALIDATION OF THE LAZARIANPOGOSYAN FARADAY-SCREEN THEORY

In this chapter we confront the analytic predictions derived previously with direct measurements obtained from a fully three-dimensional magneto–hydrodynamic (MHD) simulation of an isothermal, compressible, magnetised turbulent slab with resolution 256^3; sonic Mach number $M_\mathrm{s} = 0.8$; Alfvénic Mach number $M_\mathrm{A} = 1.0$.

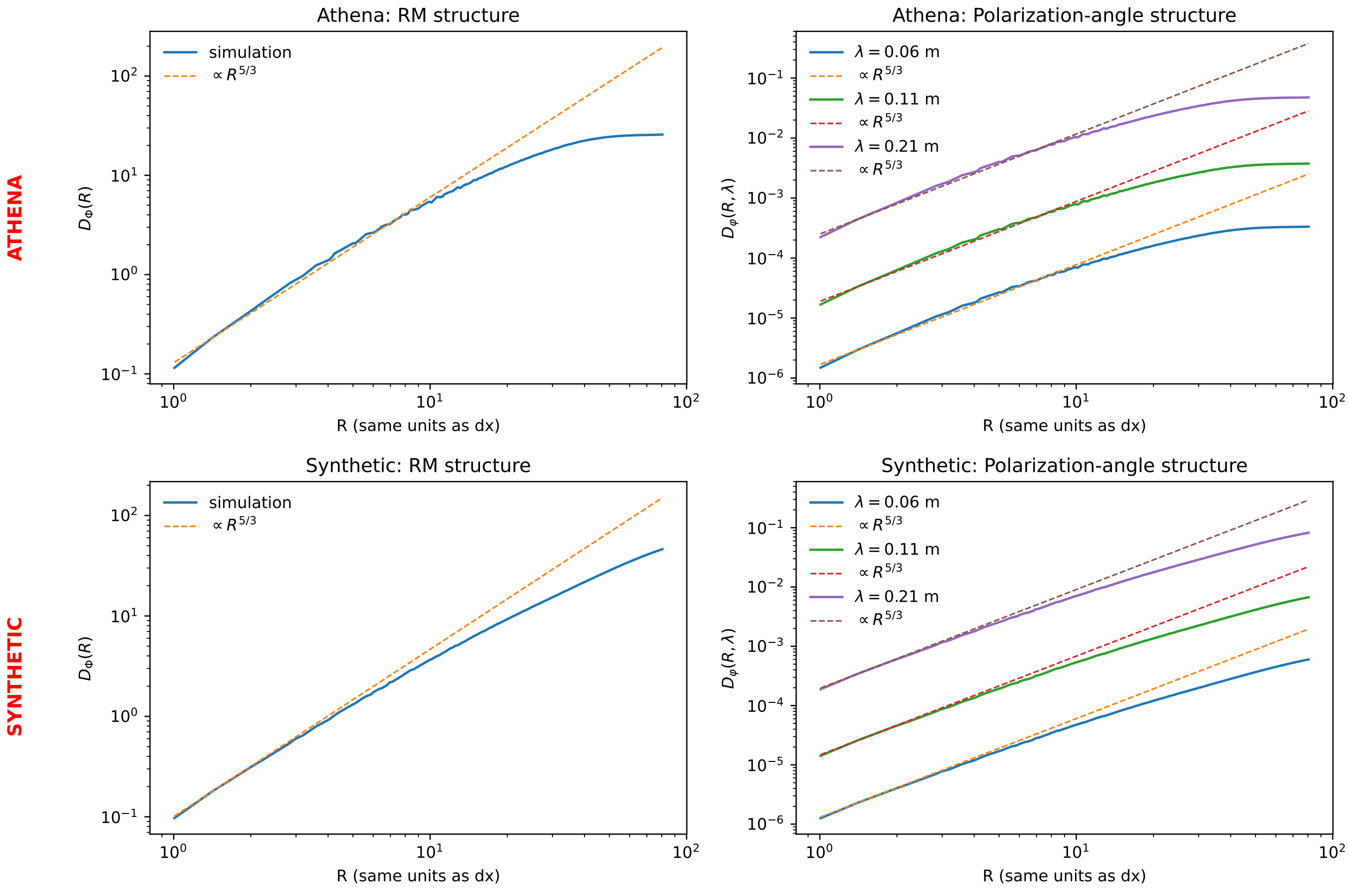

Figure 4. [

RM and angle structure functions] **Top:** Athena generated code. **Bottom:** Kolmogorov synthetic cube. **Left:** Structure function of the line-of-sight rotation measure, $D_\Phi(R) = \langle [\Phi(\mathbf{X}+\mathbf{R}) - \Phi(\mathbf{X})]^2 \rangle$, computed from the RM map integrated through the simulation cube. A reference $R^{5/3}$ slope (orange dashed) is over-plotted. **Right:** Polarisation-angle structure function $D_\varphi(R,\lambda)$ for three wavelengths (blue, orange, green). In the inertial range the curves inherit exactly the same $5/3$ exponent and diverge vertically as $\propto \lambda^4$, in agreement with Eq. (10).

10. OVERCOMING LARGE ANGLES SATURATION BY USING NEARBY FREQUENCIES.

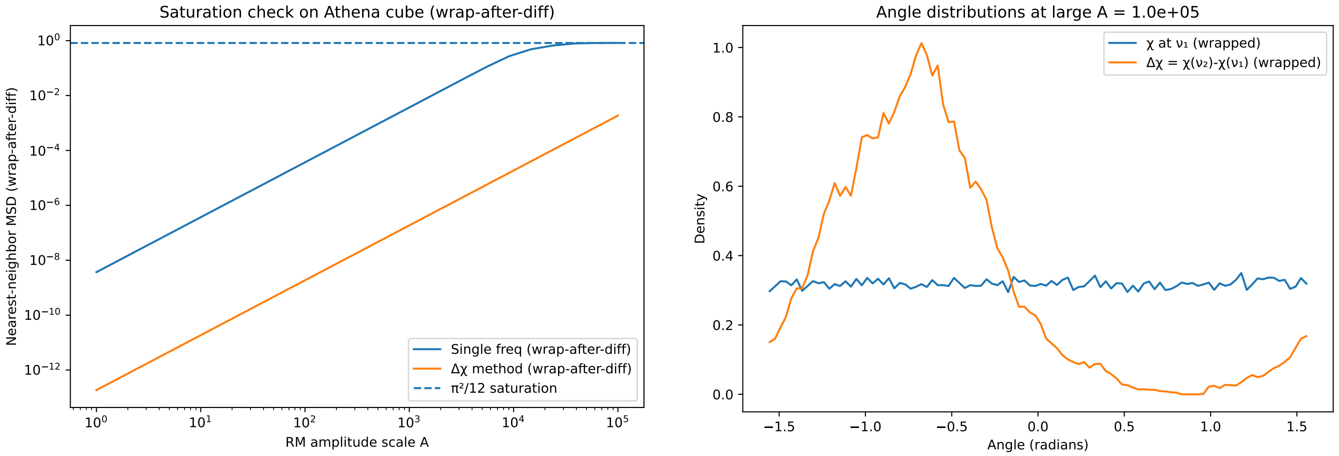

Figure 5. Left: Nearest-neighbor mean squared difference of polarization angles versus RM amplitude scale factor A for Athena cube. Right: PDF of the χ for both $\chi(\nu_1)$ and $\Delta\chi = \chi(\nu_2) - \chi(\nu_1)$. For the regular $\chi(\nu_1)$ the density was the same for the whole interval, while for $\Delta\chi$ there were a local maximum at -0.22π and min at around 0.27π.

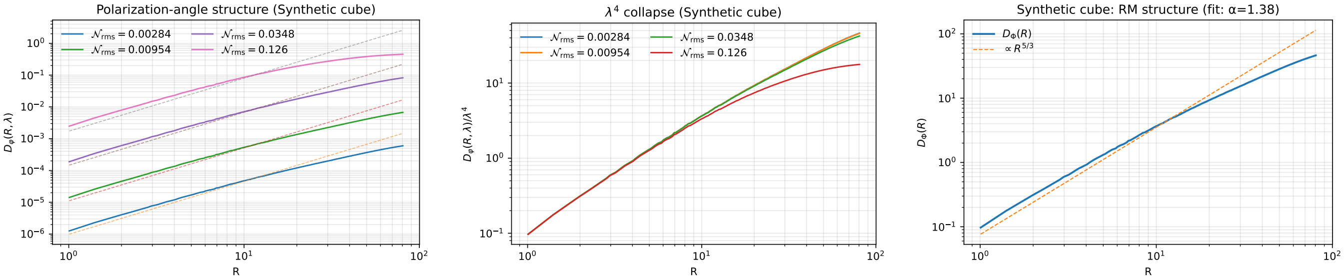

Figure 6. Left: Polarization-angle structure functions $D_\phi(R,\lambda)$ across wavelengths, showing high-ν (halo-dominated), intermediate (λ^4 scaling), and low-ν (saturated) regimes. The number of the full turns of the polarization vector was calculated with $\mathcal{N}_{\rm RMS}(\lambda) = \frac{\lambda^2 \sigma_\Phi}{2\pi}$. Central: Polarization angle structure function linearized by the λ^4, shows a better linear correlation for smaller wavelength. Right: Rotation-measure structure function $D_\Phi(R)$ from the Faraday screen, with $R^{5/3}$.

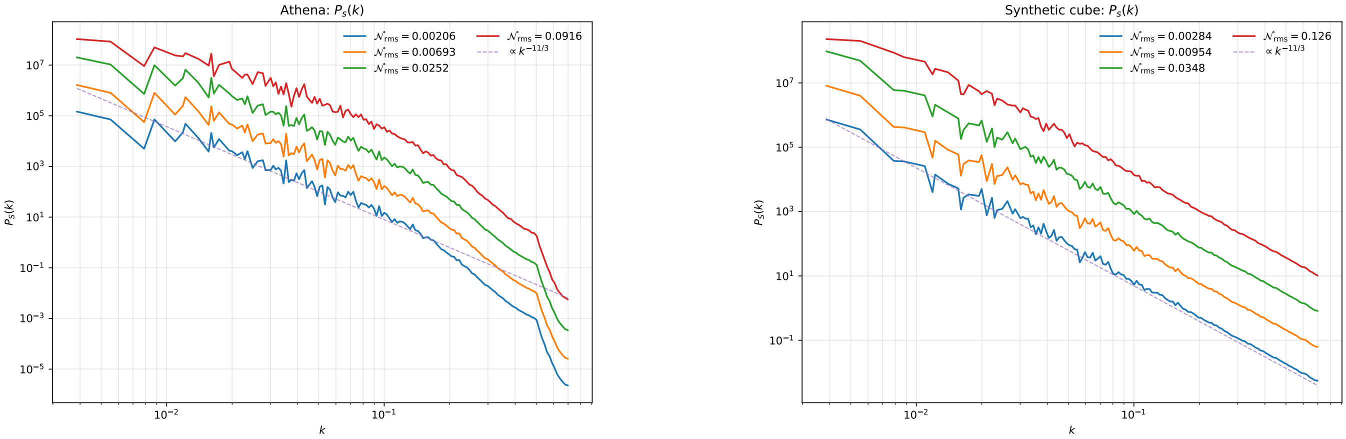

Figure 7. Fourier power spectra $P_s(k)$ of $\langle \cos 2f_1 \cos 2f_2 + \sin 2f_1 \sin 2f_2 \rangle$

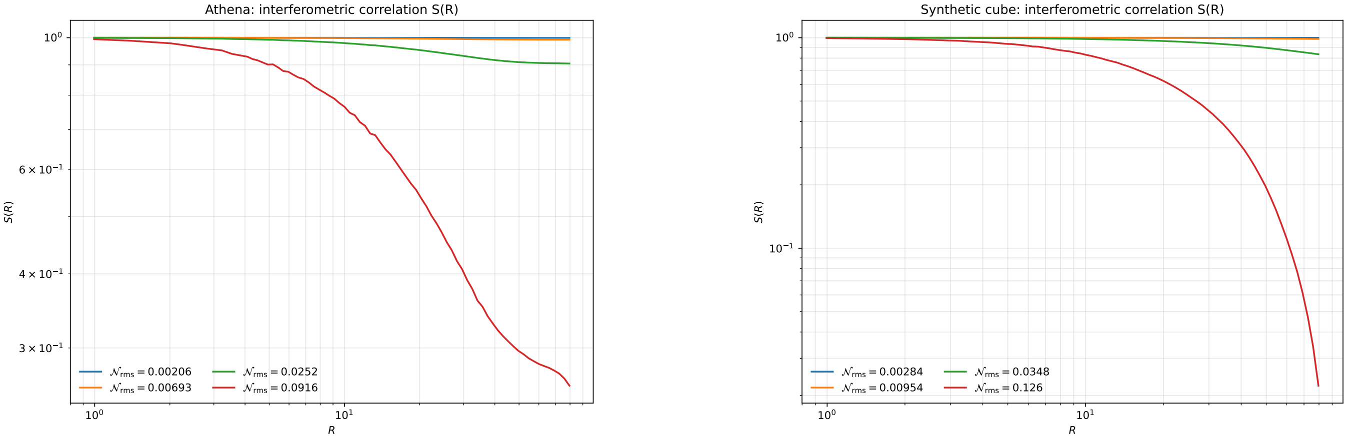

Figure 8. Real space correlation $S(R) = \langle \cos 2(f_1 - f_2) \rangle$, obtained by IFFT of $P_s(k)$ and normalized to $S_{\rm max} = 1$.

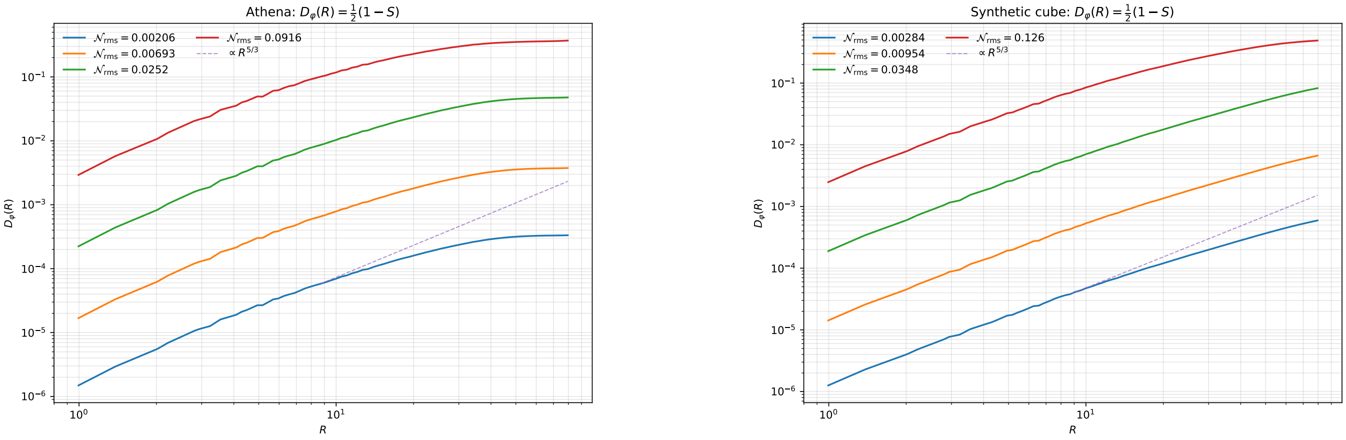

Figure 9. Structure function $D_\phi(R) = \frac{1}{2}\left[1 - S(R)\right]$

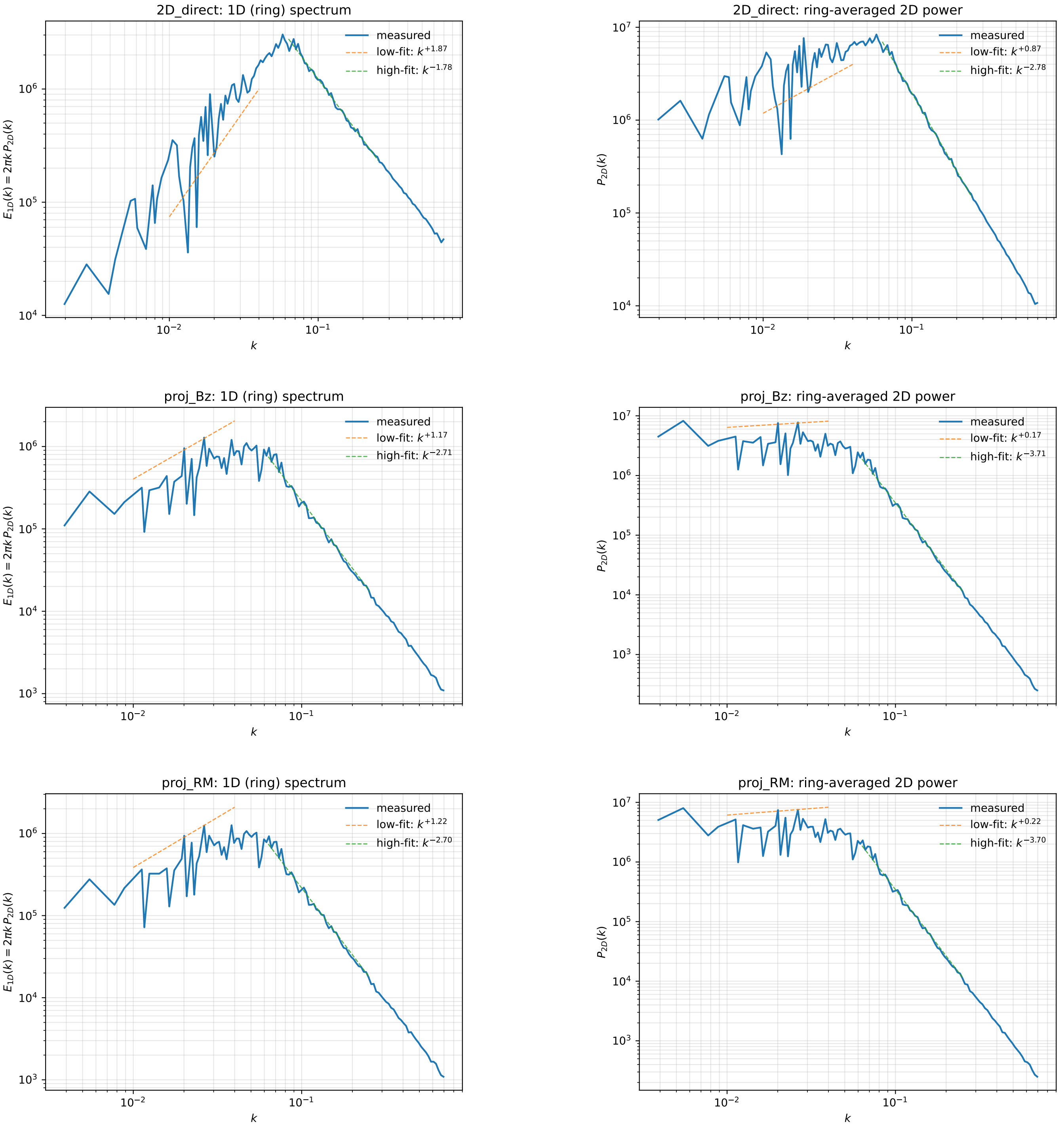

Figure 10. Power spectra of the synthetic two-slope fields. Top row: direct 2D realization, Middle row: projected B_z map from the 3D cube, Bottom row: projected Faraday-screen map $\int n_e B_z dz$. Left column: one-dimensional energy spectra $E_{1\mathrm{D}}(k) = 2\pi k P_{2\mathrm{D}}(k_x, k_y)$. Right column: two-dimensional power spectra $P_{2\mathrm{D}}(k_x, k_y)$.

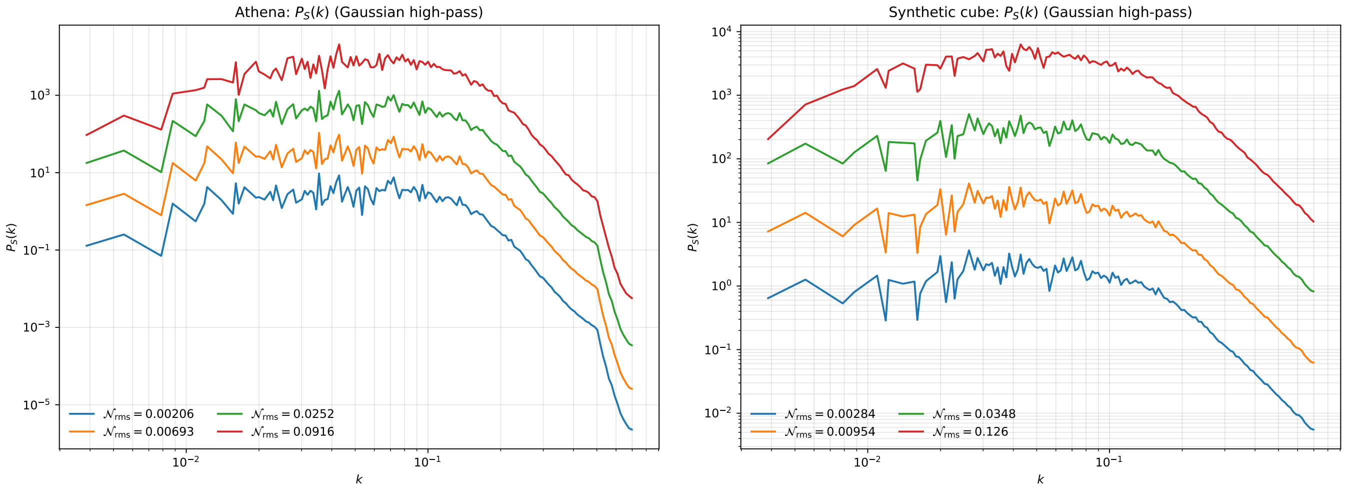

Figure 11. Applied Gaussian High-Pass $H_{\rm hp}(k) = 1 - \exp\left(-\frac{k^2}{2k_c^2}\right)$. Fourier power spectra $P_s(k)$ of $\langle \cos 2f_1 \cos 2f_2 + \sin 2f_1 \sin 2f_2 \rangle$

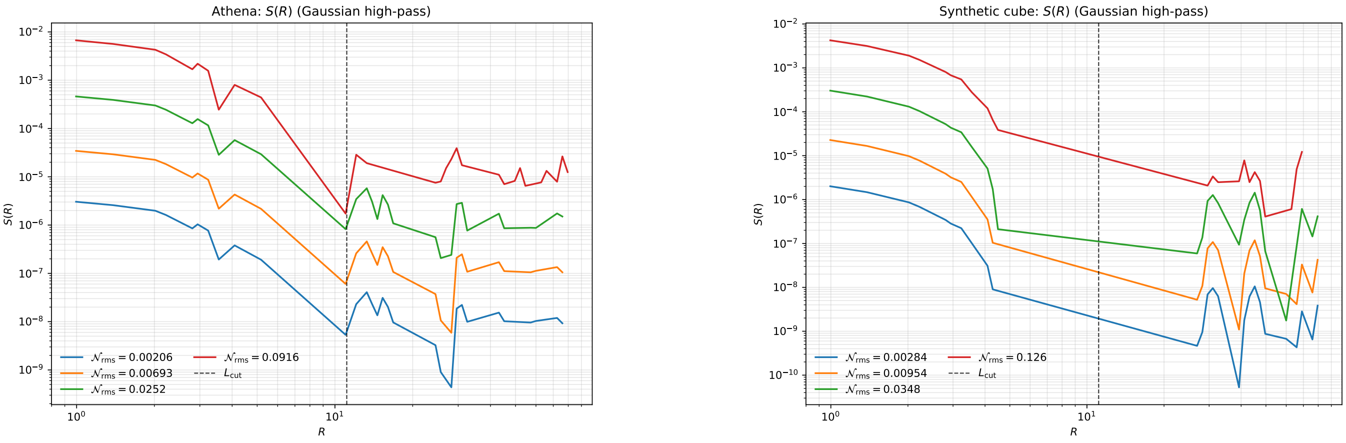

Figure 12. Gaussian high pass applied for $k_c = 0.02$. real space correlation $S(R) = \langle \cos 2(f_1 - f_2) \rangle$, obtained by IFFT of $P_s(k)$ and normalized to $S_{\rm max} = 1$.

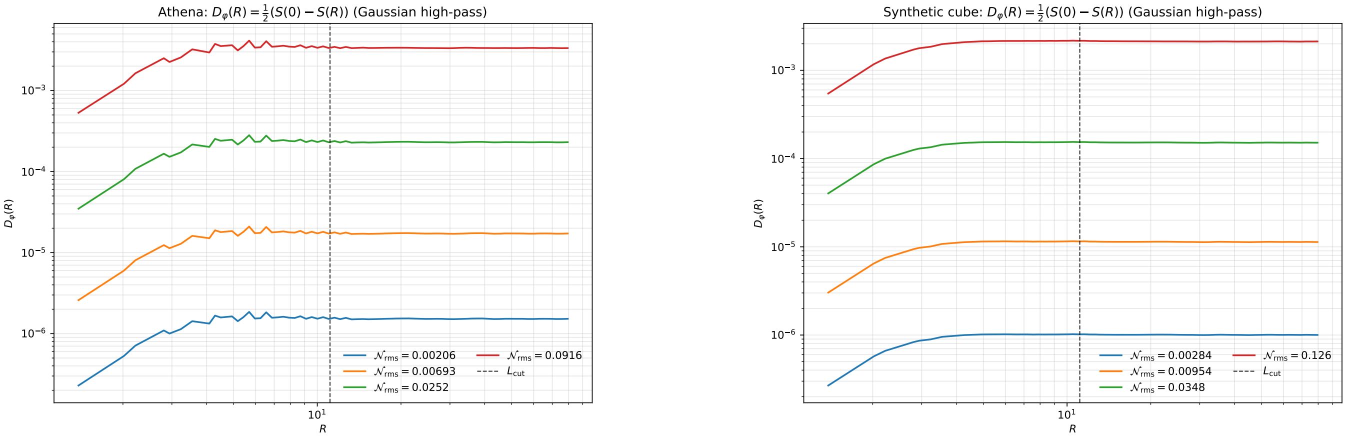

Figure 13. Gaussian high pass applied. Structure function $D_\phi(R) = \frac{1}{2}\left[S(0) - S(R)\right]$

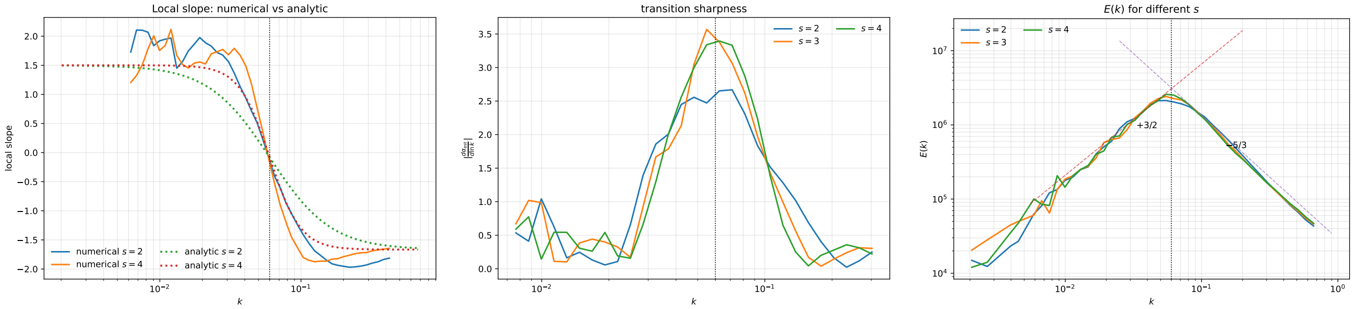

Figure 14. Dependence of the energy spectrum from the transition coefficient s

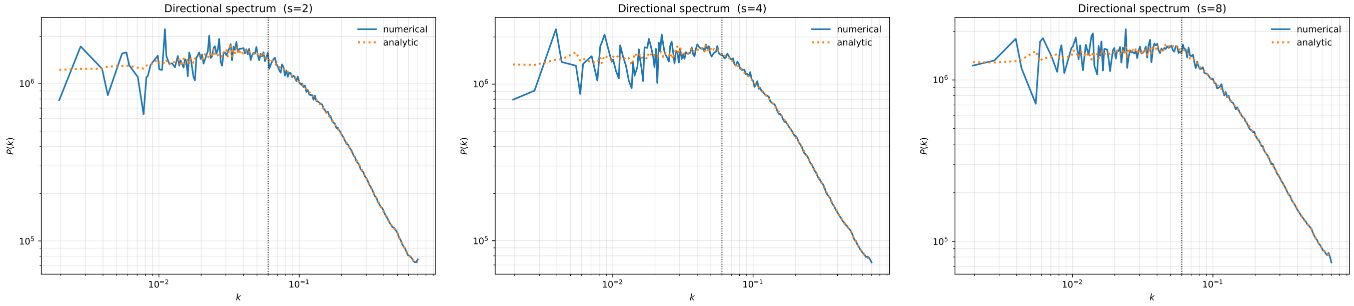

Figure 15. Spectrum obtained from $|\widehat{\cos 2f}|^2 + |\widehat{\sin 2f}|^2$ on the 2D grid; dotted curve is the analytic by the FFT of $S_+^{\rm ana}(R)$ (multiplied by the number of pixels).

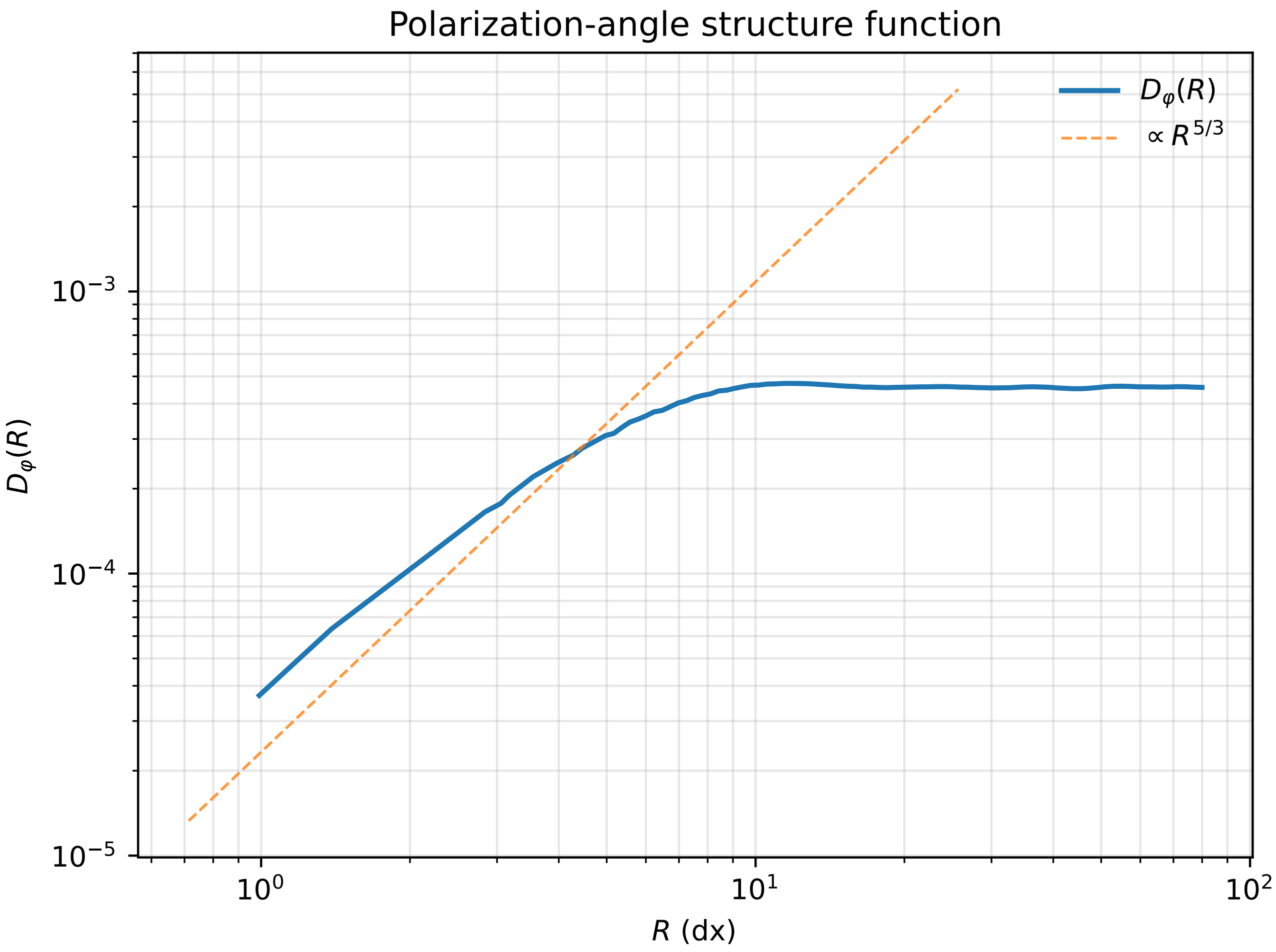

Figure 16. Polarization angle structure function

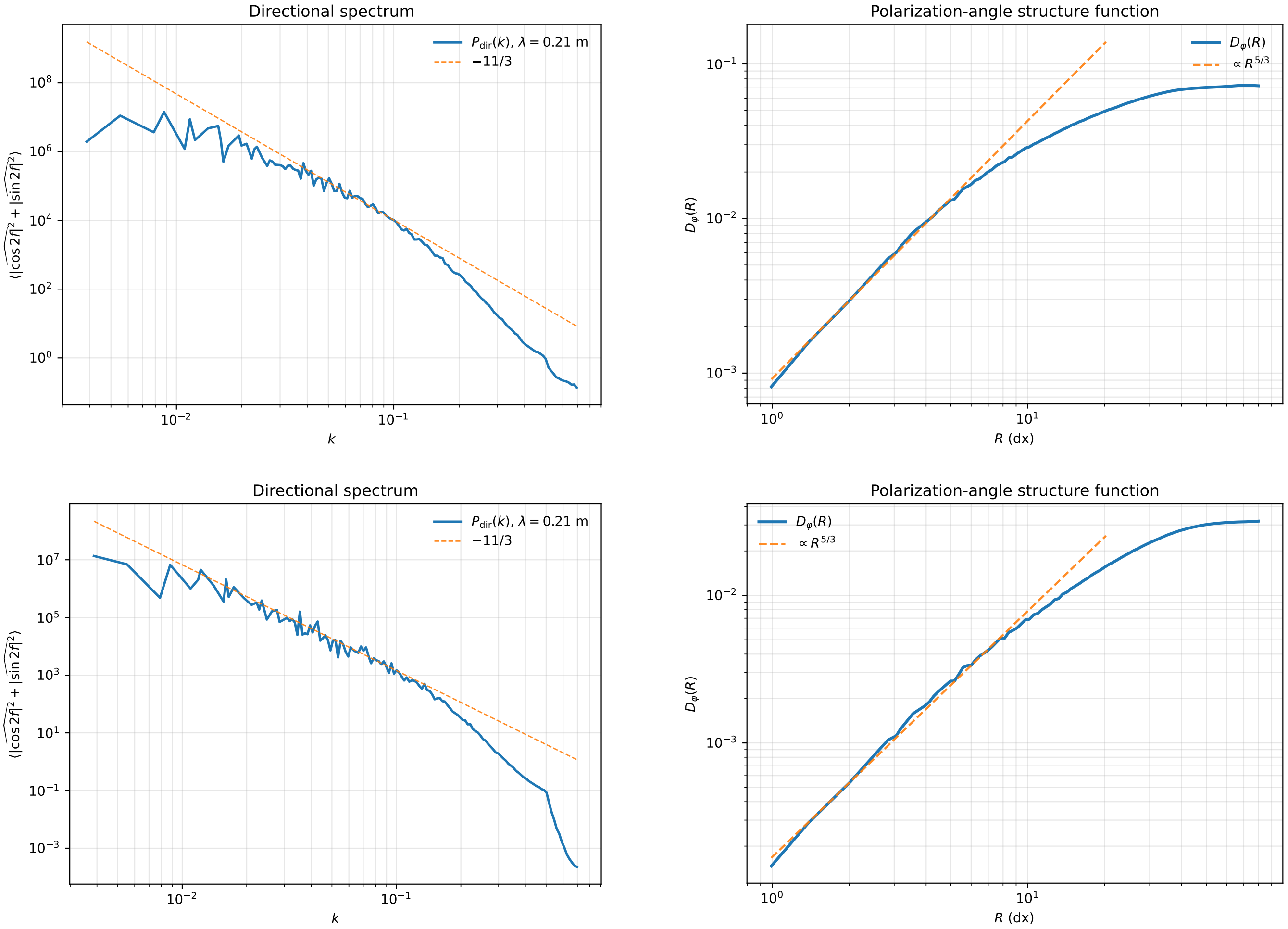

Figure 17. Top: Polarization angle structure function and the directional spectrum for the Athena snapshot $M_{\rm A} = 2.0$ and $M_{\rm s} = 0.2$. Bottom: for the Athena snapshot $M_{\rm A} = 0.8$ and $M_{\rm s} = 1.0$.

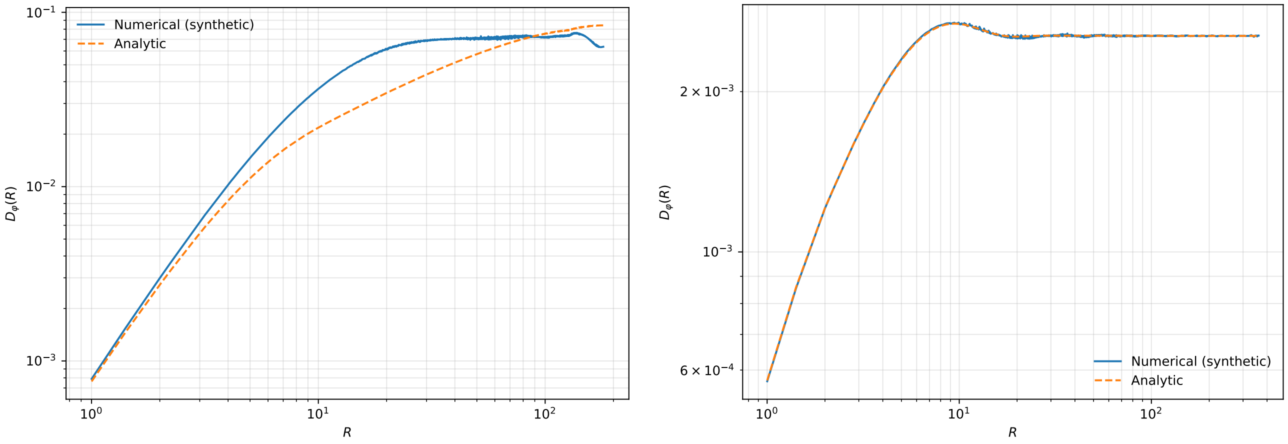

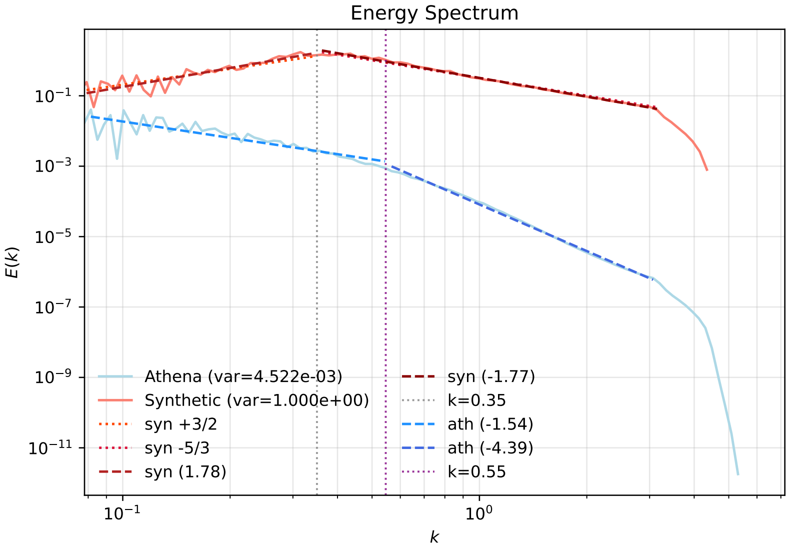

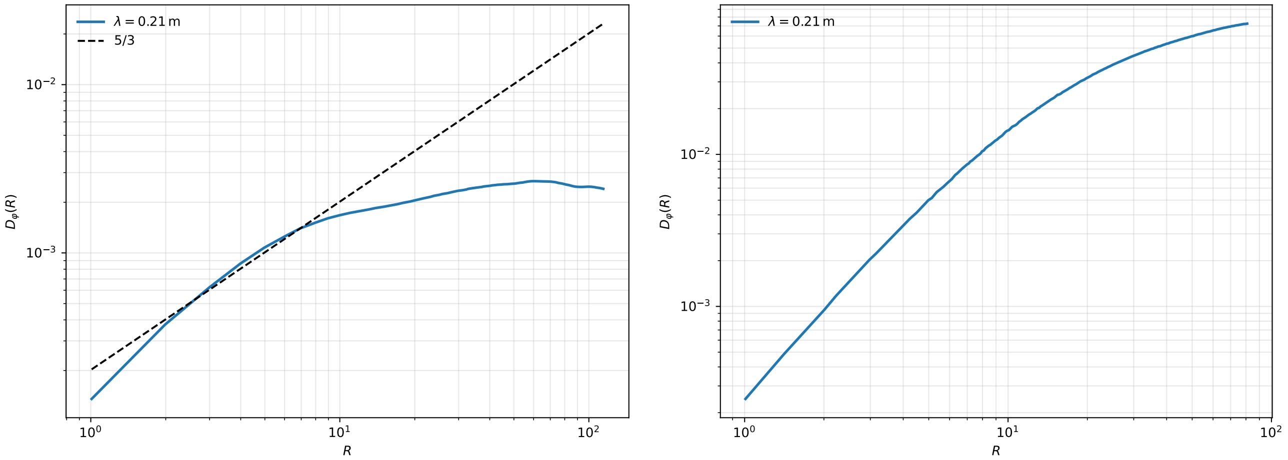

Figure 18. Left: Polarization angle structure function for the synthetic cube with $\alpha_{\rm low}=0$, $\alpha_{\rm high}=-5/3$. Right: Polarization angle structure function for the synthetic cube with $\alpha_{\rm low}=1.5$, $\alpha_{\rm high}=-5/3$.

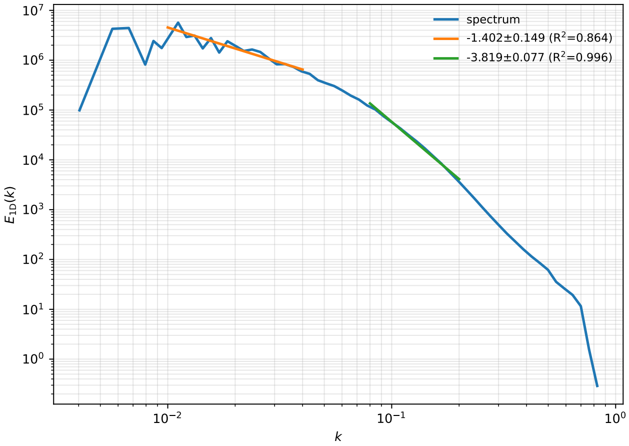

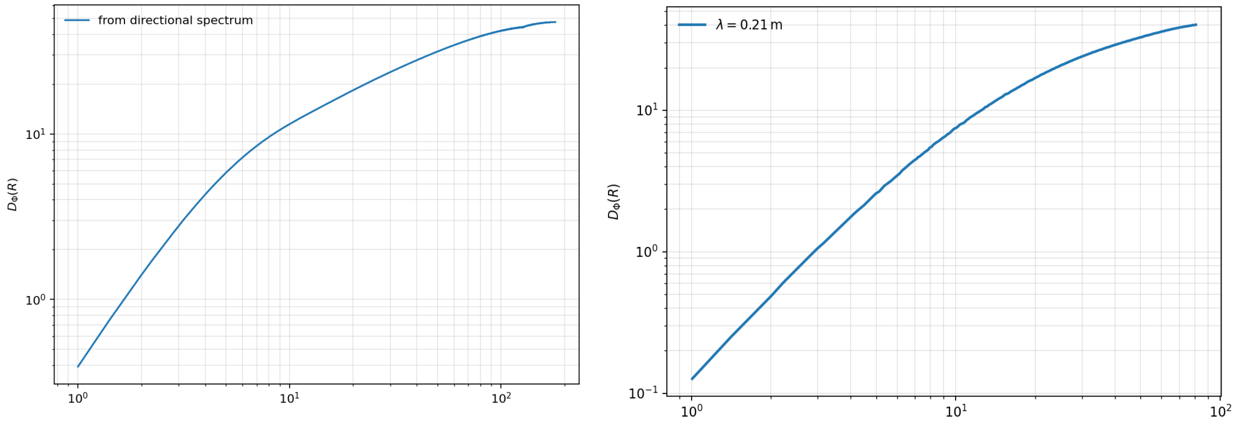

Figure 19. Left: D_Φ for energy spectrum, right: D_Φ for directional spectrum

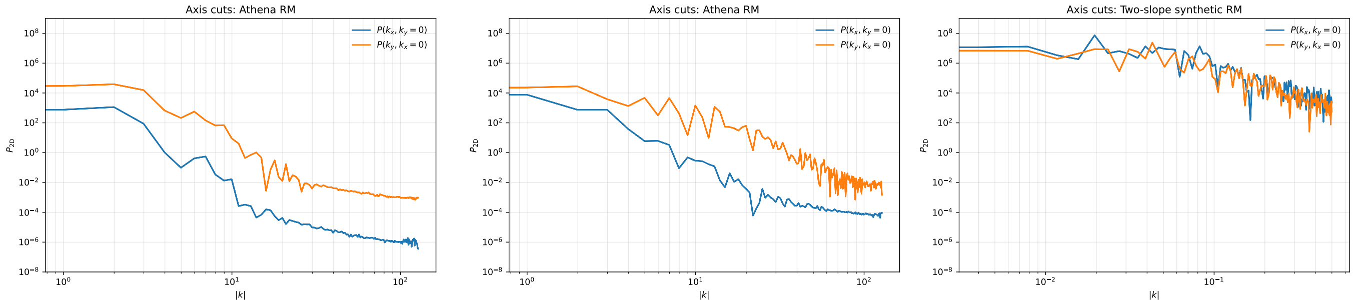

Figure 20. Left: Axis-parallel slices of the 2D RM power spectrum from the Athena map for for $t = 5.8$s, Center: Athena for $t = 11.7$s Right: Axis-parallel slices of the 2D RM power spectrum from the two-slope synthetic map

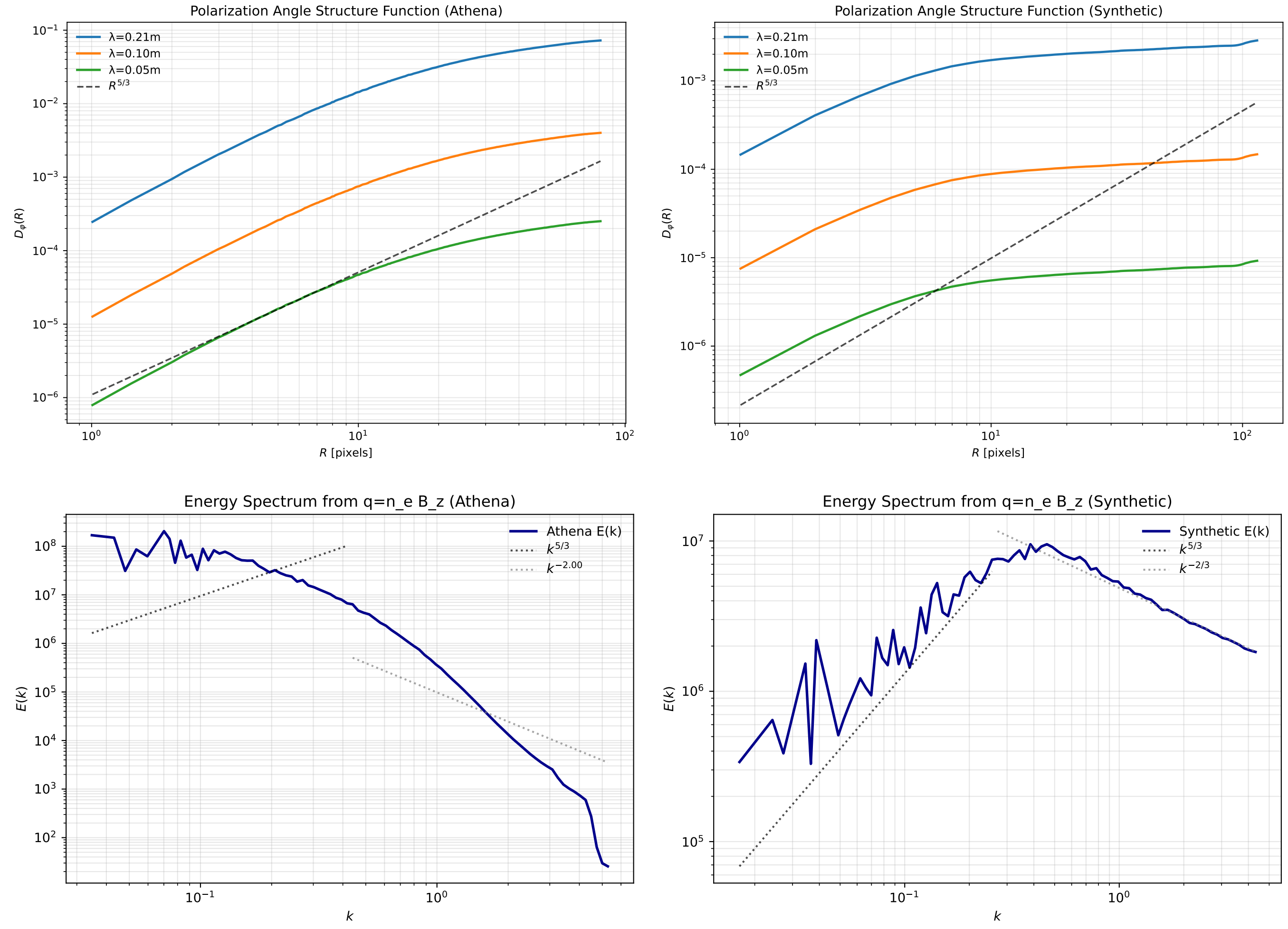
Polarization Angle Structure Function (Athena)
λ=0.21m
λ=0.10m
λ=0.05m
$R^{5/3}$
$D_\varphi(R)$
R [pixels]
10^{-1}
10^{-2}
10^{-3}
10^{-4}
10^{-5}
10^{-6}
10^0
10^1
10^2
Polarization Angle Structure Function (Synthetic)
λ=0.21m
λ=0.10m
λ=0.05m
$R^{5/3}$
$D_\varphi(R)$
R [pixels]
10^{-3}
10^{-4}
10^{-5}
10^{-6}
10^0
10^1
10^2
Energy Spectrum from q=n_e B_z (Athena)
Athena E(k)
$k^{5/3}$
$k^{-2.00}$
$E(k)$
k
10^8
10^7
10^6
10^5
10^4
10^3
10^2
10^{-1}
10^0
Energy Spectrum from q=n_e B_z (Synthetic)
Synthetic E(k)
$k^{5/3}$
$k^{-2/3}$
$E(k)$
k
10^7
10^6
10^5
10^{-1}
10^0

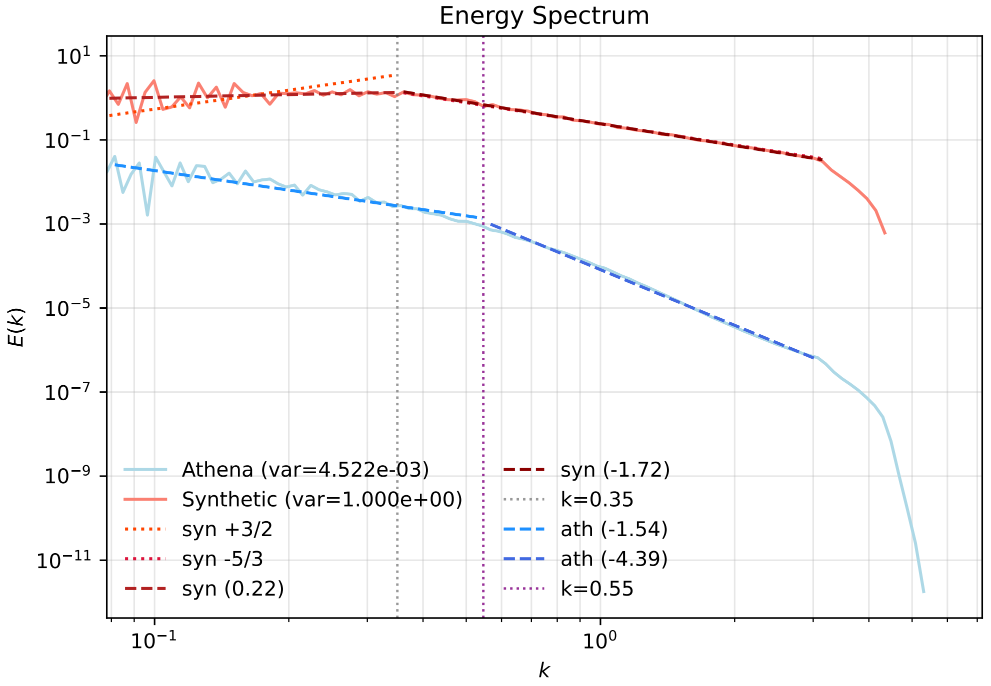
Energy Spectrum
$E(k)$
k
10^1
10^{-1}
10^{-3}
10^{-5}
10^{-7}
10^{-9}
10^{-11}
10^{-1}
10^0
Athena (var=4.522e-03)
Synthetic (var=1.000e+00)
syn +3/2
syn -5/3
syn (0.22)
syn (-1.72)
k=0.35
ath (-1.54)
ath (-4.39)
k=0.55

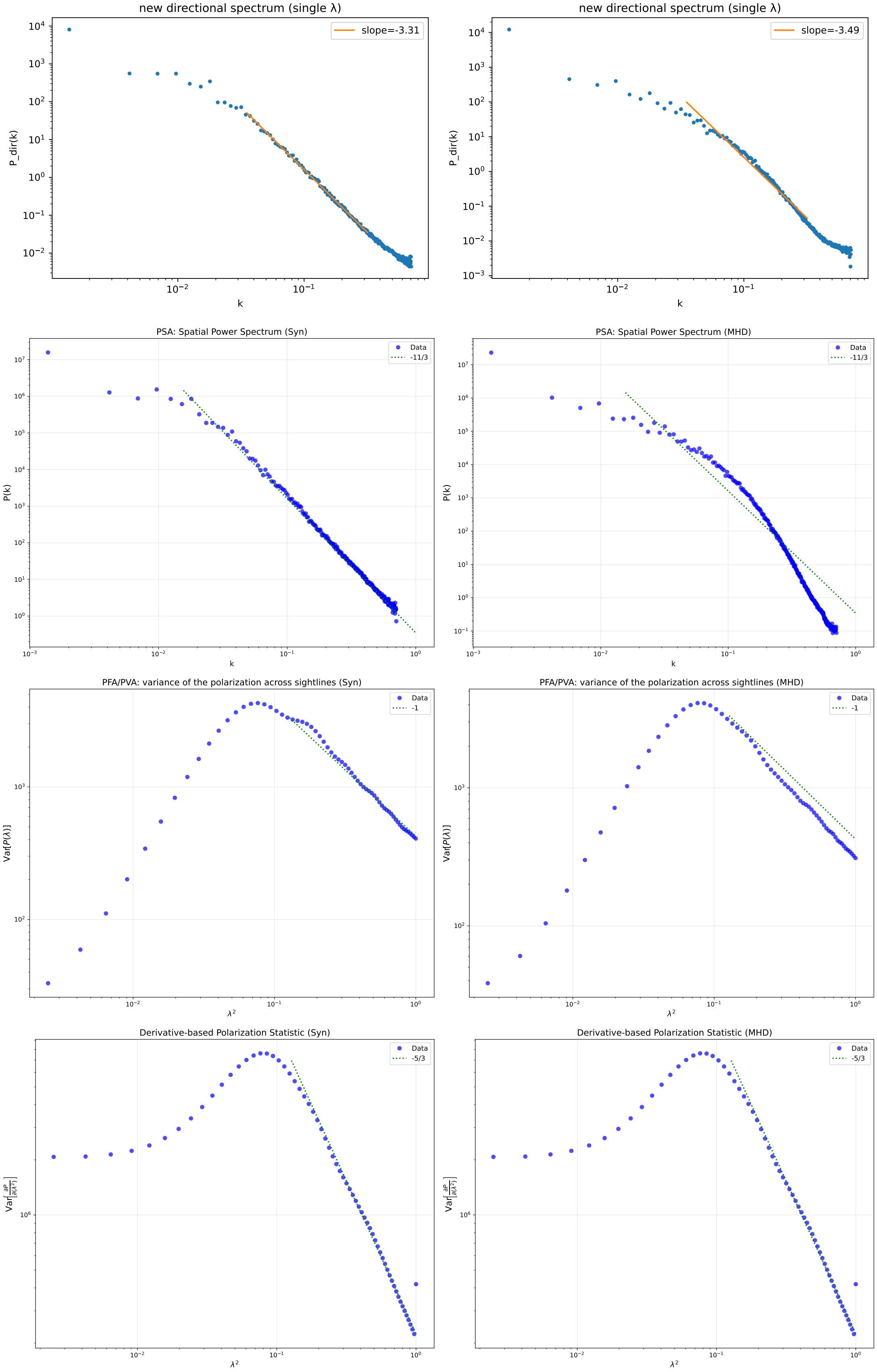

Figure 21. Comparison of turbulence measures ($\lambda = 0.21$) for (left) a synthetic screen and (right) an sub-Alfvenic MHD snapshot ($M_{\rm A} = 0.8$). Top row: Directional spectrum $P_{\rm dir}(k)$ traces angle fluctuations and is Faraday-sensitive at larger λ^2. Second row: PSA (Polarization Spatial Analysis) $|\widehat{P}(k)|^2$ at the same λ is typically emission-dominated when rotation is weak, revealing the synchrotron and magnetic spectral slope. Third row: Polarization Faraday Analysis (PFA)/Polarization Variance Analysis (PVA) ${\rm Var}[P(\lambda)]$ vs λ^2 exhibits regime changes (mean-field vs fluctuation-dominated Faraday) via slope breaks. Bottom row: Derivative ${\rm Var}[\partial P/\partial(\lambda^2)]$.

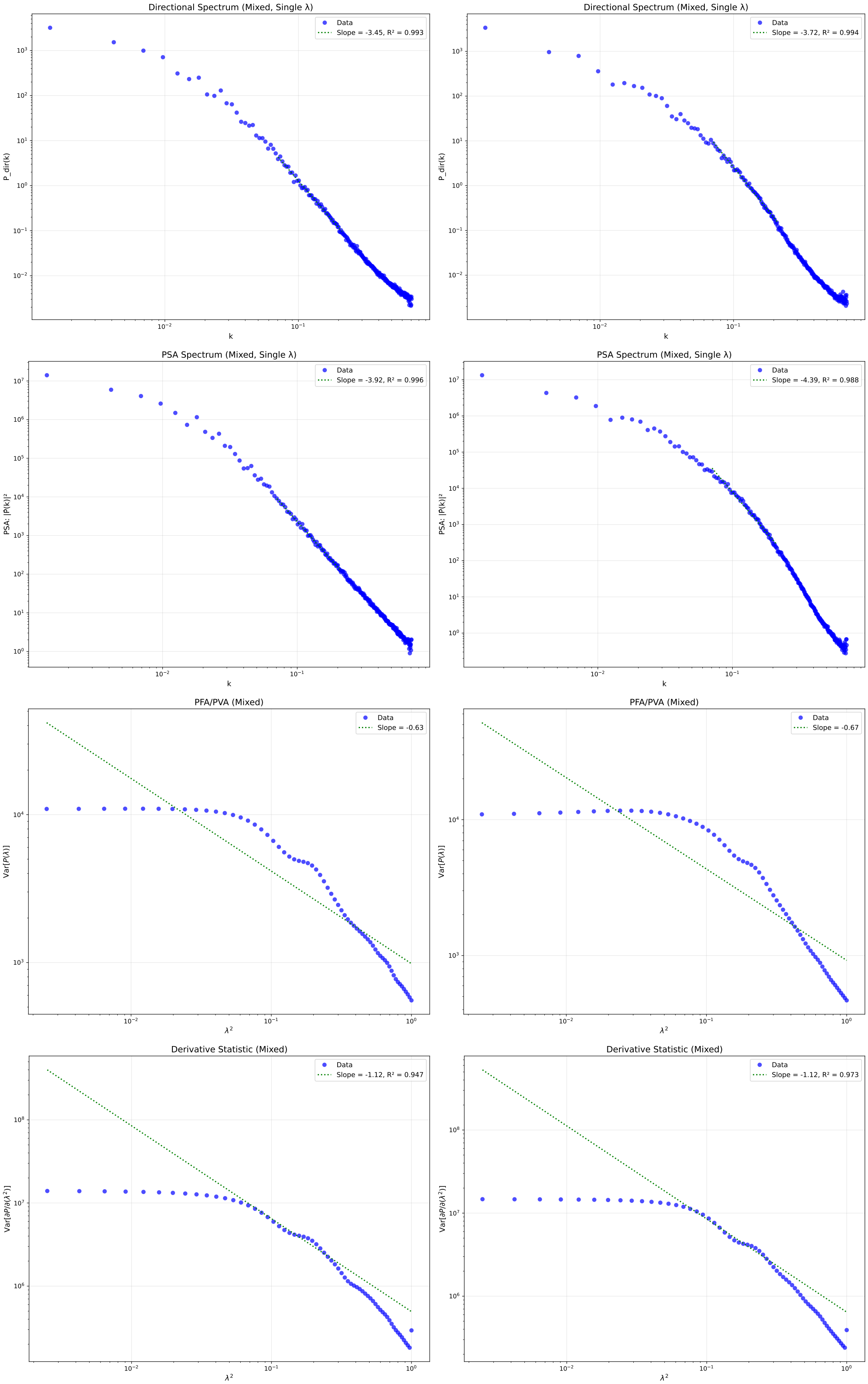

Figure 22. Comparison of measures in the regime were synchrotron emission and Faraday rotation are co-spatial, shown for a synthetic field (left) and an MHD cube (right). Top row: directional spectra. Second row: Polarization Spatial Analysis (PSA) spectra. Third row: Polarization Faraday Analysis (PFA) variance versus λ^2. Bottom row: derivative statistics.

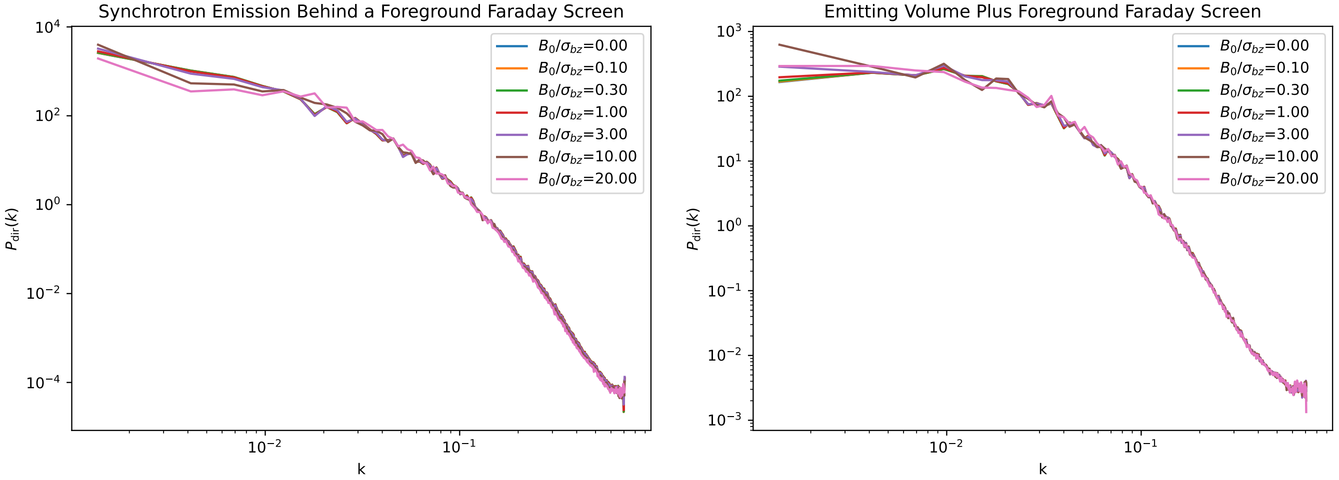

Figure 23. Polarization power spectra for two configurations: (Left) Synchrotron-emitting gas without internal Faraday rotation, viewed through a foreground Faraday screen; only the screen's line-of-sight magnetic field rotates the polarization. (Right) Synchrotron-emitting gas that both emits and internally rotates due to its own line-of-sight magnetic field, with an additional foreground Faraday screen in front.

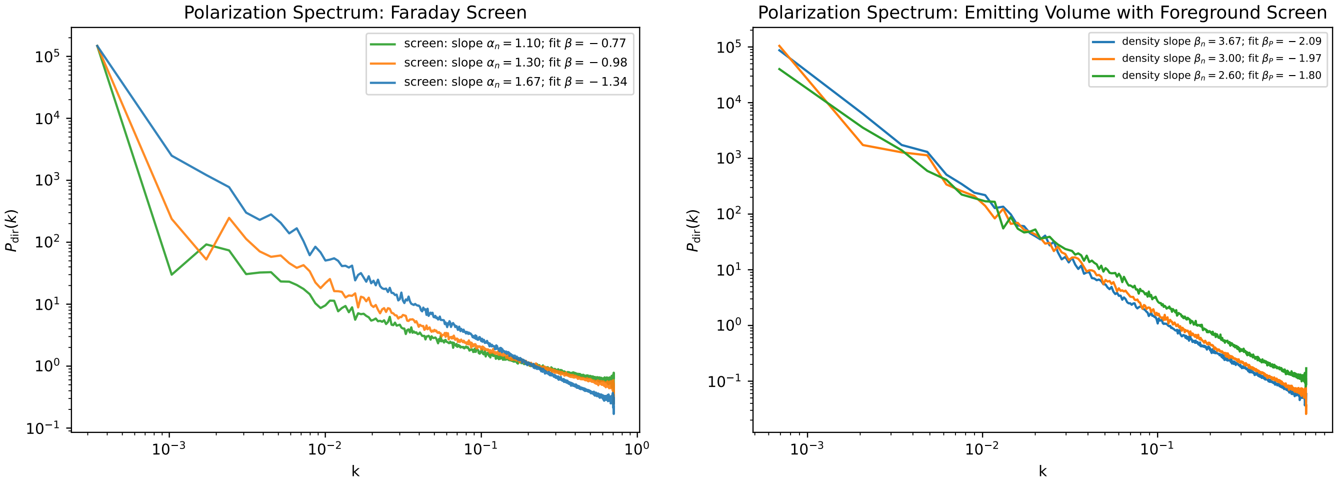

Figure 24. Polarization power spectra for two cases: (left) a background signal rotated by a Faraday screen, and (right) an emitting volume that both emits and rotates due to its internal magnetic field, with an additional foreground Faraday screen.

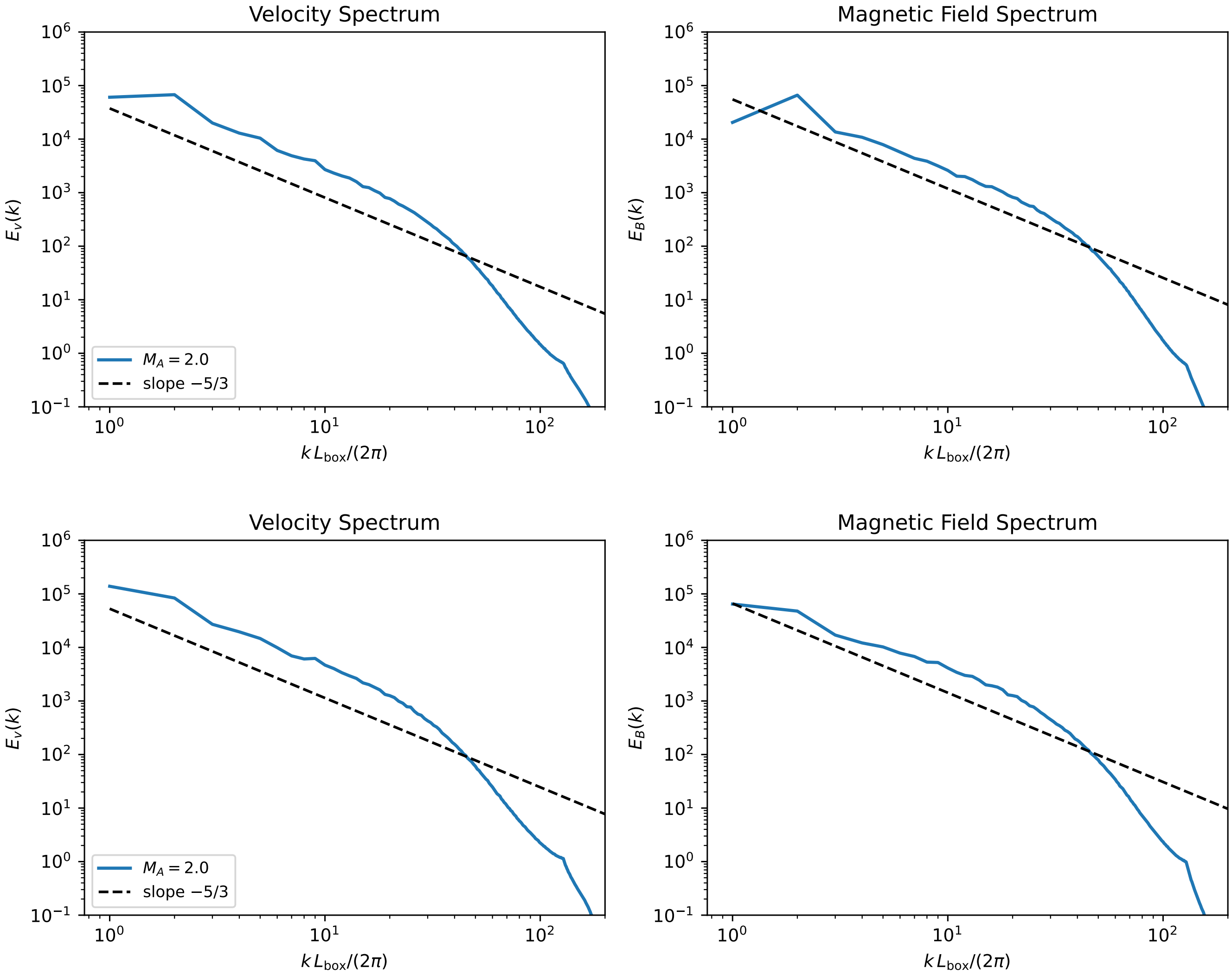

Figure 25. Spectra of velocity (left) and magnetic field under different M_A conditions (M_A=0.8 top, M_A=2 bottom). The dashed line represents the expected scaling for Kolmogorov turbulence $E_k \sim k^{-5/3}$ over the inertial range.